

UNIVERSIDAD SANTIAGO DE CHILE
FACULTAD DE CIENCIAS
Departamento de Física



Electron transport in driven nanojunctions.

Felipe Alexis Recabal Rivas

Profesor Guía:

Felipe Herrera Urbina

Proyecto de Título para optar al grado
académico de Magíster en Ciencia con
Mención en Física.

Santiago de Chile, Chile

2021

Acknowledgement

This work was funded by:

- National Agency for Research and Development (ANID) through Becas de Magíster Nacional 2020 - 22200493.
- Iniciativa Científica Milenio (ICM) through the Millennium Institute for Research in Optics (MIRO).

Resumen

Nanojunturas ofrecen la posibilidad de estudiar las propiedades de transporte de materiales nanométricos impulsados, como puntos cuánticos o moléculas individuales, unidos a cables eléctricos. Recientes estudios experimentales y teóricos de estos sistemas han aumentado nuestro entendimiento de procesos de transporte cuántico, que subyace el comportamiento de los bloques de construcción de circuitos electrónicos.

En esta Tesis, estudiamos el transporte de electrones en nanojunturas. Desarrollamos un modelo en el cual la nanojuntura es tratada como un sistema cuántico abierto, con el material nanométrico modelado como un arreglo conductor de sitios de electrones, interactuando con múltiples ambientes. Modelamos la dinámica de la nanojuntura con una ecuación maestra cuántica de Lindblad, que toma en consideración las interacciones que inducen transiciones de electrones entre los autoestados del arreglo conductor. Resolviendo numéricamente la dinámica de la nanojuntura en el estado estacionario, calculamos observables de la nanojuntura como la corriente eléctrica a través de la nanojuntura mientras un voltaje de polarización es aplicado.

Nuestros resultados muestran que la dinámica de tuneldeo de electrones explica picos de conductancia a voltajes donde la condición de resonancia es satisfecha. Procesos como emisión espontánea y relajación por fonones, explica el comportamiento de las poblaciones para un conjunto de autoestados afectados por ellos, produciendo que sus contribuciones a la corriente en los contactos a la izquierda y derecha sean diferentes. El transporte de electrones es dependiente de la geometría del arreglo conductor, pero alcanzando un valor similar de corriente de saturación. Cuando una fuente de bombeo incoherente es aplicada al arreglo conductor, nuestros resultados muestran los efectos de luz inducida por corriente y corriente inducida por luz, permitiendo inclusive una corriente fotoeléctrica a configuraciones donde el voltaje de polarización es cero cuando las tasas de tuneldeo a la izquierda y derecha son diferentes, mientras que dirección de la corriente fotoeléctrica inducida depende de si el arreglo conductor tiene electrones deslocalizados en el conjunto de orbitales base o el excitados.

Palabras claves: Juntas moleculares, puntos cuánticos, sistemas cuánticos abiertos, transporte de electrones, ecuación maestra cuántica.

Abstract

Nanojunctions offer the possibility of studying the transport properties of driven nano-sized materials, such quantum dots or single molecules, attached to electric leads. Recent experimental and theoretical studies of these systems has increasing our understanding of quantum transport phenomena, that underlie the behaviour of the building blocks of electronic circuits.

In this Thesis, we study the electron transport in nanojunctions. We develop a model in which the nanojunction is treated as an open-quantum system, whit the nano-sized material modelled as a conducting array of electron sites, interacting with multiple environments. We model the nanojunction dynamics with a Lindblad quantum master equation, which takes into account the interactions that induce electron transitions between the conducting array eigenstates. Solving numerically the nanojunction dynamics in the steady state, we compute nanojunction observables such as the electric current through the nanojunction while a bias voltage is applied.

Our results show that electron tunneling dynamics explains conductance peak at voltages where a resonant condition is satisfied. Processes such as spontaneous emission or phonon relaxation, explain the behaviour of populations on a set of eigenstates affected by them, producing that their contribution to the current at the left-right contacts are different. Electron transport is dependent on the conducting array geometries, but reaching similar saturation current value. When an incoherent pumping source is applied to the conducting array, our results show the effects of current-induced light and light-induced current, allowing even a photocurrent at zero bias configuration when the left-right tunneling rates are different, while the induced photocurrent direction depends on whether the conducting array has delocalized electrons in the ground or the excited orbital manifold.

Key words: Molecular junctions, quantum dots, open-quantum systems, electron transport, quantum master equation.

Contents

1	Introduction	1
1.1	Quantum dots	1
1.2	Molecular junctions	3
1.3	Quantum transport phenomenology	4
2	Nanojunction description	9
2.1	Density operator formalism	10
2.1.1	Quantum-mechanical systems	10
2.1.2	Populations and coherences	11
2.1.3	Reduced density operators	11
2.1.4	Thermal-equilibrium density operators	12
2.2	Model nanojunction	13
2.2.1	Second quantization theory	14
2.2.2	Conducting array	15
2.2.3	Environment	17
2.2.4	Interactions	19
3	Nanojunction dynamics	23
3.1	Quantum master equation	23
3.1.1	Rate equations	26
3.2	Nanojunction characterization	28
3.2.1	Current-voltage	28
3.2.2	Gate voltage	30
4	Results	31
4.1	Electron transition processes	32
4.1.1	Resonant tunneling	32
4.1.2	Spontaneous emission	35
4.1.3	Phonon relaxation	36
4.2	Geometry array dependence	37
4.3	Incoherent pumping	46
	Conclusions	52

Bibliography	54
Appendix	58
A Redfield equation	59
B Lindblad quantum master equation	61
C Reservoir particles evolution	65

List of Tables

4.1	Model parameters	32
4.2	Eigenstates for a single-level conducting array with spin.	34
4.3	Eigenstates for a two-level conducting array.	36
4.4	Eigenstates for a two-site conducting array	36
B.1	System and reservoir part of interaction Hamiltonians.	62
B.2	Effective transfer rates.	64

List of Figures

1.1	Vertical and lateral quantum dot structures.	6
1.2	Experimental techniques of molecular junctions.	7
1.3	Reported quantum electron transport processes.	8
2.1	Scheme of macroscopic metals and molecular junction.	9
2.2	Model of nanojunction.	13
3.1	Scheme of open-quantum system treatment and the dynamics induced in the quantum system.	25
3.2	Conducting array dynamics induced by the electron tunnelling with the leads.	28
4.1	Nanojunction for one level conducting array and time-dependent dynamics induced by resonant tunnelling.	33
4.2	Electron transport in nanojunction of one level conducting array.	39
4.3	Electron transport in nanojunction of one degenerated spin level conducting array.	40
4.4	Nanojunction and electron transport of two level conducting array.	41
4.5	Microscopic effect of spontaneous emission.	41
4.6	Nanojunction and electron transport of two level conducting array.	42
4.7	Microscopic effect of phonon relaxation.	42
4.8	Nanojunction and electron transport of geometric conducting arrays	43
4.9	Microscopic effect on geometry.	44
4.10	Electron transport in nanojunction with circular symmetrical and non-symmetrical geometry.	45
4.11	Effect of incoherent pumping on electron transport of nanojunction where the conducting array is delocalized in the excited level.	47
4.12	Microscopic effect of incoherent pumping on conducting array delocalized in the excited level at zero bias voltage.	50
4.13	Effect of incoherent pumping on electron transport of nanojunction where the conducting array is delocalized in the excited level.	51

Chapter 1

Introduction

Based on the progress of different experimental techniques and theoretical methods, nano-sized materials attached to leads, i.e. nanojunctions, have received substantial interest in the last decades as a route for studying non-equilibrium many-body quantum physics at the nanoscale [[Thoss and Evers, 2018](#)]. Experiments have shown that many of these nano-sized materials behave as “quantum dots”, where the electrons are confined in the space and described by discrete quantum states [[Andergassen et al., 2010](#)]. The quantum description of nanojunctions explains a plethora of interesting transport phenomena, which could be the basis of future applications because of the promised reduction of energy consumption, increasing capability and cheaper manufacturability of electronic circuits [[Sowa et al., 2017](#)].

This Chapter gives a brief introduction to nanojunctions, focusing on quantum dots and molecular junction devices, which are some of the most studied systems. Basic definitions are also explained.

1.1 Quantum dots

Quantum dots are low-dimensional system where a few conduction electrons are trapped. The name refers to devices where electrons are confined in the three spatial dimensions. The typical size of quantum dot varies between 1 to 100 nanometers, which contains from 10^3 to 10^6 atoms with equivalent number of electrons. The confinement produces that only few electrons are free, while the other are bounded to the atomic nucleus [[Tartakovskii, 2012](#), [Kouwenhoven et al., 1997](#)]. Because of the small size of quantum dots, these free electrons are distributed in discrete quantum states and have a charging energy for adding a new electron, analogous to the ionization potential in atoms. Therefore quantum dots has been considered as “artificial atoms”, while multiple coupled quantum dots have been considered as “artificial molecules” [[Kouwenhoven, 1995](#)].

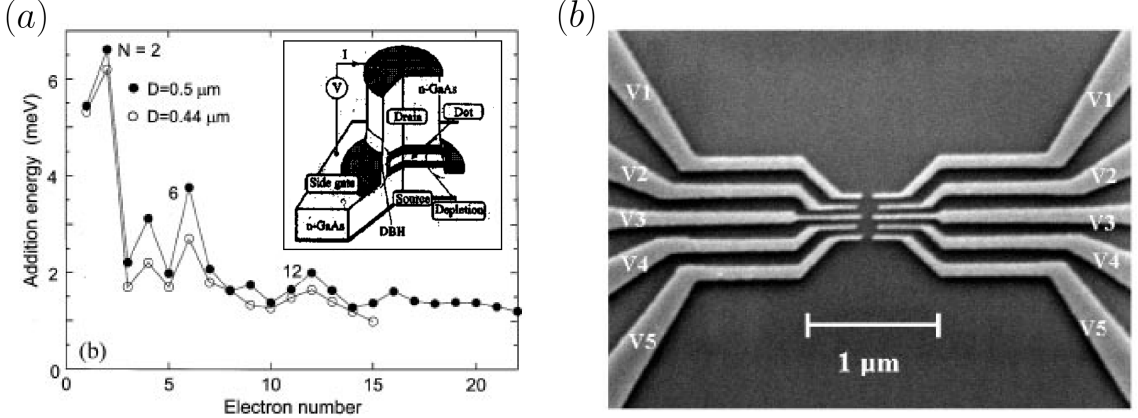


Figure 1.1: (a) Addition energy as a function of electron number N of vertical quantum dot with diameters D (inset: vertical quantum dot structure composed semiconductor materials, where could be applied a voltage V and a gate voltage); (b) coupled quantum dot in a lateral structure, where ten independently tunable gates squeeze the electron gas formed by the GaAs/AlGaAs heterostructure. Panels (a) and (b) adapted from [Tarucha et al., 1996] and [Jeong et al., 2001], respectively.

In vertical quantum dots, structure formed by etched pillars of semiconductor materials where the quasi-two-dimensional island of electron is squeezed by gate voltage applied through the metallic side around the vertical structure (see inset in Fig. 1.1(a)), the current as a function of gate voltage for small bias voltage has shown that the excess energy for charging the quantum dot from N to $N + 1$ electrons follows the filling of 2D harmonic potential, where the big peaks at $N = 2, 6$ and 12 represent the close shell structure, while the filling of the middle region is consequence of alignment Hund's rules, as is shown in Fig. 1.1(a), analogous to atomic ionization spectra [Tarucha et al., 1996, Reimann and Manninen, 2002].

For studying electron transport, a common way to fabricate quantum dots or coupled quantum dots is to deposit gates over a two-dimensional electron gas formed by a mesoscopic semiconductor heterostructure (typically GaAs/AlGaAs), where the electrostatic effect of an applied voltage by the gates tend to electrostatically create a bowl-like potential, which confines the electron in the lateral direction [Reimann and Manninen, 2002], as in shown in Fig. 1.1(b). Therefore, the quantum dot is limited to a small region of a semiconductor material of typical size of 100 nanometers [Kouwenhoven et al., 1997].

Quantum dots are used for studying many-body properties of a finite fermionic systems with scope on areas such as chemistry, medicine and material science, based on the possibility of register current and voltage leads as a function of electrostatic gates, dot geometry or magnetic field [Tartakovskii, 2012, Reimann and Manninen, 2002].

1.2 Molecular junctions

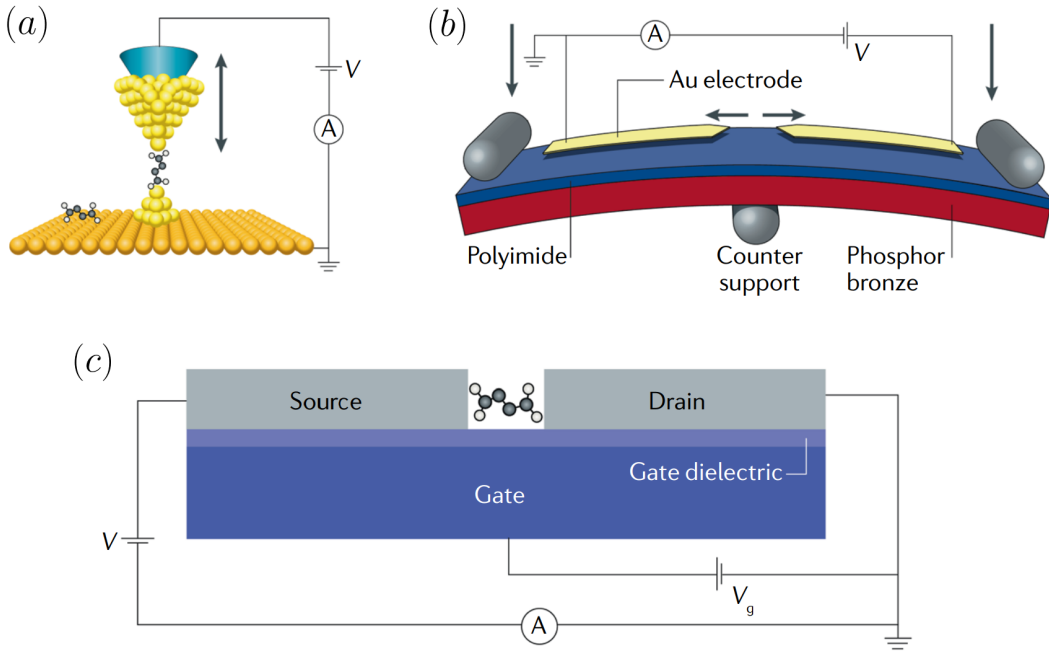


Figure 1.2: Techniques of molecular junction fabrication, where a bias voltage (V) is applied while current is measured (A); (a) Scanning tunneling microscope break junction; (b) Mechanically controllable break junctions; and (c) Electromigration break junctions, which offer the possibility of adding a gate voltage (V_g). Adapted from [Gehring et al., 2019].

Molecular junctions refers to system in which a single molecule, as small as one nanometer, is placed between two metallic or semiconductor leads, measuring its transport properties [Evers et al., 2020]. Its development has been framed in a field called *molecular electronics*, which studied electronic and thermal transport in circuits composed by individual molecules, and has allowed to answer basic questions and quantum phenomena [Scheer and Cuevas, 2017, Thoss and Evers, 2018].

Transport through single molecules was theoretically first proposed by Aviram and Ratner at 1974 [Aviram and Ratner, 1974], but it was not until 1997, based on techniques for the development of metallic wires at the end of the 1980's and the beginning of the 1990's, in [Reed et al., 1997, Scheer and Cuevas, 2017] the first experiment of single molecule were done, showing the rectifier behaviour theoretically predicted. To date, the most frequent techniques to implement molecular junctions are [Gehring et al., 2019, Evers et al., 2020]:

- Scanning tunneling microscope break junction: The tip of an STM is pushed repeatedly on the metallic substrate, where molecules are deposited, and retracted, as is shown in Fig. 1.2(a). The gap formed between the tip and the substrate is small enough to bridge molecules, which are measured as the conductance as a function of distance while a bias voltage is applied.

- Mechanically controllable break junctions: A notched or lithographically fabricated metallic wire is deposited on the top of a flexible substrate. The system is bending, using a three point mechanism, until the wire breaks, as is shown in Fig. 1.2(b). The gap in controlled relaxing the bending while evaporated single molecule in the environment could be attached to the leads, measured as a non-zero current.
- Electromigration (EM) break junctions: A metal wire is deposited over a dielectric using lithography techniques, where an applied voltage rampe creates by electromigration¹ a gap small enough to form a bridge for a single molecule, as is shown in Fig. 1.2(c). Molecules could be deposited onto the wire before or after the electromigration. Unlike with the other techniques, EM break junctions offer the possibility of adding a third gate, which add an electrostatic effect by a gate voltage V_g .

1.3 Quantum transport phenomenology

In this thesis, we discuss the following quantum transport phenomena:

- Coulomb blockade: In a three gate system, when a gate voltage induces an electrostatic change of the quantum dots or single molecule energies continuously, it could be charged by the electrons tunneled from the leads, measured as a conductance peak at small bias voltage. Coulomb blockade occurs when the addition of a single-electron is avoided if the charging energy is greater than the thermal energy [Reimann and Manninen, 2002, Tartakovskii, 2012]. At the Coulomb blockade regime, the conductance peaks of a single electron tunneling looks as periodic oscillations, known as Coulomb oscillations [Kouwenhoven et al., 1997], as is shown in Fig. 1.3(a).
- Kondo effect: At low temperatures is appreciate of some conductance peaks arise due to the Coulomb interaction of opposite spins in the same state [Yoffe, 2001]. When the conductance is measured as a function of temperature in the middle region between the peaks, a non-monotonic behaviour of resistance is produced, as is shown in Fig. 1.3(b), first reported by Kondo in metals containing magnetic impurities [Kondo, 1964]. The Kondo effect has been attributed to the strong correlations between spin electrons at low temperature, and has been reported in molecular junctions and quantum dots. For bulk material, the Kondo effect decreases the transport because it increases the electron scattering by the impurities, while in quantum dots or molecular junctions it enhances the transport, because of the electron are transport only through these electron sites [Inoshita, 1998].

¹The electromigration is the process where conducting electron driven a diffusion of atoms under large current.

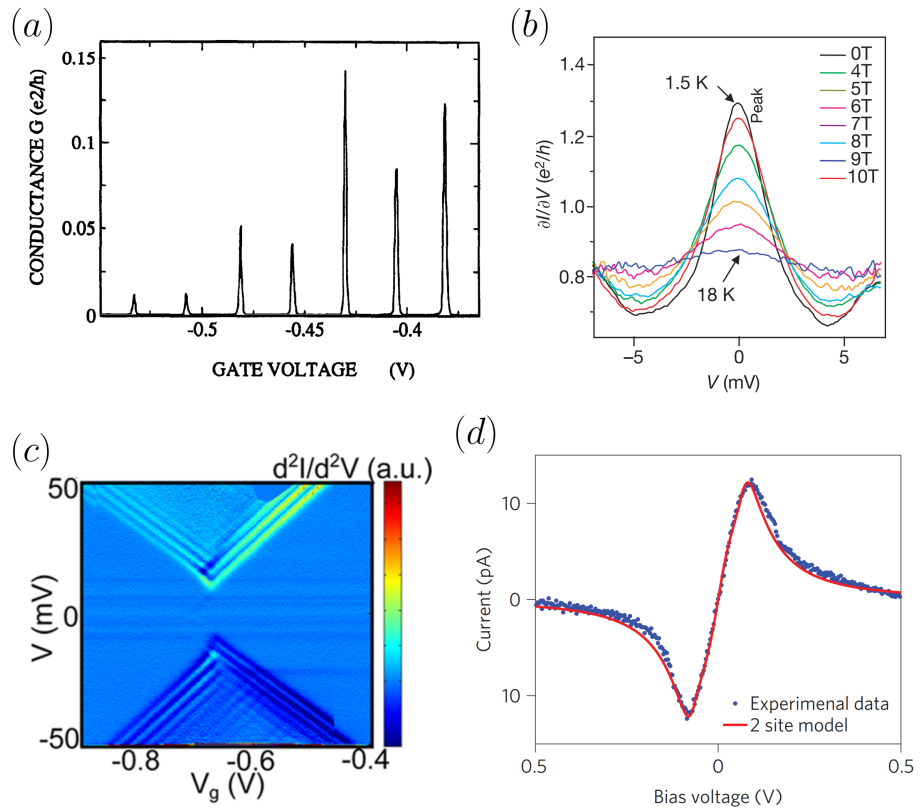


Figure 1.3: Reported quantum transport phenomena; (a) conductance as a function of gate voltage at zero bias voltage for a quantum dot system, which shows Coulomb oscillations; (b) conductance as a function of gate voltage at different temperatures for a molecular junction system, which shows a Kondo peak; (c) derived conductance as a function of gate voltage and bias voltage for a molecular junction system, which shows Franck-Condon blockade; and (d) current-voltage curve for a molecular junction system, which shows negative differential conductance. Panels (a), (b), (c) and (d) adapted from [Kouwenhoven et al., 1991], [Park et al., 2002], [Burzurí et al., 2014] and [Perrin et al., 2014], respectively.

- Franck-Condon blockade: When the electrons are strongly coupled to a vibrational mode, the transport properties are affected. In the Franck-Condon blockade, single-electron tunneling is suppressed at low bias for any gate voltage, as is shown in Fig. 1.3(c), and has been reported in molecular junctions [Burzurí et al., 2014] and carbon nanotube [Leturcq et al., 2009].
- Negative differential conductance: Negative differential conductance corresponds to an effect where the electron current decreases while a bias voltage increases over a specific range, as is shown in Fig. 1.3(d). It was first reported in p-n junctions and semiconductor heterostructures, but also appears in quantum dots and molecular junction systems [Xue et al., 1999]. This has been attributed to narrow feature of the density of states of the tip apex atom in STM [Xue et al., 1999], conformational changes, spin blockade, phonon blockade or suppressed resonant transport [Perrin et al., 2014].

Nanojunction description

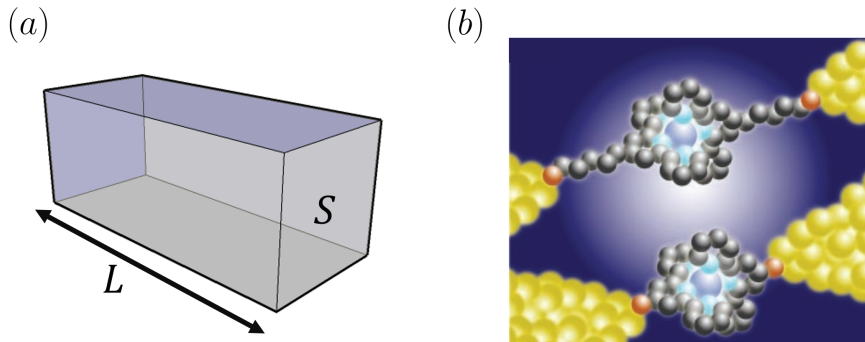


Figure 2.1: Scheme of (a) macroscopic metal; and (b) molecular junction. Panel (b) adapted from [Nitzan and Ratner, 2003].

In macroscopic metals, the conductance G follows the Ohm law according to

$$G = \sigma \frac{S}{L}, \quad (2.1)$$

where σ is the conductivity, S is the traversal area and L is the length, as is shown in Fig. 2.1(a). Nevertheless, in nanojunctions, because of the size of the attached material, for example the single molecule in Fig. 2.1(b), the electron transport happens in the quantum regime, which produces, in general, non-Ohmic behaviour [Scheer and Cuevas, 2017]. It means, this kind of systems need to be described as a quantum system.

This Chapter develops a quantum description of nanojunctions, based on the density operator approach and the second quantization formalism. The nanojunction is modelled, capturing or ignoring some electron transfer processes.

2.1 Density operator formalism

In this work the system is described by a density operator, because of the system dynamics is reduced to a compact and reduced number of equations for many-particle systems and macroscopic observables [Breuer et al., 2002, Nitzan, 2006].

2.1.1 Quantum-mechanical systems

A quantum-mechanical system is described by a wave function $|\Psi(t)\rangle$, which evolves through the Schrödinger equation ($\hbar = 1$),

$$\frac{d}{dt} |\Psi(t)\rangle = -i\hat{\mathcal{H}} |\Psi(t)\rangle, \quad (2.2)$$

where $i = \sqrt{-1}$ is the imaginary unit and $\hat{\mathcal{H}}$ is the system Hamiltonian. Writing the Hamiltonian $\hat{\mathcal{H}}$ in diagonal form as

$$\hat{\mathcal{H}} |\phi_n\rangle = \omega_n |\phi_n\rangle, \quad (2.3)$$

where $\{|\phi_n\rangle\}$ are the system eigenstates (or eigenbasis) and $\{\omega_n\}$ are the eigenenergies (or spectrum). The wave function of the system $|\Psi(t)\rangle$ can be written as

$$|\Psi(t)\rangle = \sum_n C_n(t) |\phi_n\rangle, \quad C_n(t) = \langle \phi_n | \Psi(t) \rangle, \quad (2.4)$$

where the time-dependent coefficients, $C_n(t)$, satisfy $\sum_n |C_n(t)|^2 = 1$ due the normalization of the wave function.

The average of any physical observable of the system associated to an operator $\hat{\mathcal{A}}$, based on the system wave function in Eq. (2.4), is computed as a function of time as

$$\langle \hat{\mathcal{A}} \rangle = \langle \Psi(t) | \hat{\mathcal{A}} | \Psi(t) \rangle = \sum_{n,m} C_n(t) C_m^*(t) \mathcal{A}_{m,n} \equiv \sum_{n,m} \rho_{n,m}(t) \mathcal{A}_{m,n}, \quad (2.5)$$

where $\mathcal{A}_{m,n} = \langle \phi_m | \hat{\mathcal{A}} | \phi_n \rangle$ is an element of $\hat{\mathcal{A}}$ and $\rho_{n,m}(t) = \langle \phi_n | \hat{\rho}(t) | \phi_m \rangle$ is an element of the system density operator $\hat{\rho}$, defined as

$$\hat{\rho}(t) = |\Psi(t)\rangle \langle \Psi(t)|, \quad (2.6)$$

which stores information about the system. With the density operator in Eq. (2.6), the average of the observable $\hat{\mathcal{A}}$ in Eq. (2.5) is reduced to

$$\langle \hat{\mathcal{A}} \rangle = \text{Tr} [\hat{\rho}(t) \hat{\mathcal{A}}], \quad (2.7)$$

where Tr correspond to a trace over the system space. The results above were derived using the eigenbasis $\{|\phi_n\rangle\}$, but is valid for any basis in the system space.

Based on the Schrödinger equation in Eq.(2.2) and the density operator in Eq. (2.6), the evolution of the density operator is given by the Liouville's equation,

$$\frac{d}{dt} \hat{\rho}(t) = -i [\hat{\mathcal{H}}, \hat{\rho}(t)], \quad (2.8)$$

where $[\hat{\mathcal{H}}, \hat{\rho}(t)] = \hat{\mathcal{H}}\hat{\rho}(t) - \hat{\rho}(t)\hat{\mathcal{H}}$ is the commutator.

Therefore, the density operator and the Liouville's equation are an alternative way for describing quantum-mechanical systems, while the Eq. (2.7) is a way for computing average of observables.

2.1.2 Populations and coherences

For any density operator $\hat{\rho}$, exist a basis $\{|\psi_\alpha\rangle\}$ where it takes a diagonal form, it is,

$$\hat{\rho} = \sum_{\alpha} \rho_{\alpha} |\psi_{\alpha}\rangle \langle \psi_{\alpha}|, \quad (2.9)$$

where ρ_{α} correspond to the system probability (or population) at the state $|\psi_{\alpha}\rangle$. For representing the density operator in other basis, for example the Hamiltonian basis $\{|\phi_n\rangle\}$ (see Eq. (2.3)), is used a change of basis according to

$$|\psi_{\alpha}\rangle = \sum_n a_{\alpha,n} |\phi_n\rangle, \quad a_{\alpha,n} = \langle \phi_n | \psi_{\alpha} \rangle, \quad (2.10)$$

where $a_{\alpha,n}$ are time-independent coefficients. Applying the change of basis in Eq. (2.10), the density operator in Eq. (2.9) becomes

$$\hat{\rho} = \sum_{n,m} \rho_{n,m} |\phi_n\rangle \langle \phi_m|, \quad \rho_{n,m} = \sum_{\alpha} \rho_{\alpha} a_{\alpha,n} a_{\alpha,m}^*, \quad (2.11)$$

where the terms $\rho_{n,m}$ are know as coherences when $n \neq m$ or populations when $n = m$.

2.1.3 Reduced density operators

Consider a system composed by two sub-systems \mathcal{A} and \mathcal{B} . The general form of writing the system density operator $\hat{\rho}$ in terms of the basis $\{|a\rangle\}$ and $\{|b\rangle\}$ for \mathcal{A} and \mathcal{B} sub-systems, respectively, is according to

$$\hat{\rho} = \sum_{a,b} \rho_{ab,a \cdot b} |ab\rangle \langle a \cdot b|, \quad (2.12)$$

where $\rho_{ab,a \cdot b} = \langle ab | \hat{\rho} | a \cdot b \rangle$ is an element of the density operator and the state $|ab\rangle = |a\rangle \otimes |b\rangle$ is constructed as a tensor product (\otimes) between the state $|a\rangle$ and $|b\rangle$. For an observable associated to an operator $\hat{\mathcal{A}}$ in the sub-system \mathcal{A} (see Eq. (2.7)),

$$\langle \hat{\mathcal{A}} \rangle = \text{Tr} \left[\hat{\rho} \hat{\mathcal{A}} \right] = \sum_{ab} \sum_{a \cdot b} \rho_{ab,a \cdot b} \langle a \cdot b | \hat{\mathcal{A}} | ab \rangle, \quad (2.13)$$

where Tr is the trace over the sub-systems \mathcal{A} and \mathcal{B} . Because $\hat{\mathcal{A}}$ belongs only in the space of the sub-system \mathcal{A} , the term $\langle a \cdot b | \hat{\mathcal{A}} | ab \rangle$ is reduced to $\langle a \cdot | \hat{\mathcal{A}} | a \rangle \delta_{b,b \cdot}$. Therefore, the observable in Eq. (2.13) is reduced to

$$\langle \hat{\mathcal{A}} \rangle = \sum_{ab} \sum_{a \cdot} \rho_{ab,a \cdot b} \langle a \cdot | \hat{\mathcal{A}} | a \rangle \equiv \text{Tr}_{\mathcal{A}} \left[\hat{\rho}_A \hat{\mathcal{A}} \right], \quad (2.14)$$

where $\text{Tr}_{\mathcal{A}}$ is the trace over the sub-system \mathcal{A} , and is defined the density operator of the sub-system \mathcal{A} ,

$$\hat{\rho}_A = \text{Tr}_{\mathcal{B}}[\hat{\rho}], \quad (2.15)$$

as a reduced density operator, applying the trace, $\text{Tr}_{\mathcal{B}}$, over the system density operator $\hat{\rho}$.

In the case that both sub-systems \mathcal{A} and \mathcal{B} are independent (uncorrelated), the density operator of the system could be written as a tensorial product,

$$\hat{\rho} = \hat{\rho}_A \otimes \hat{\rho}_B, \quad (2.16)$$

of,

$$\hat{\rho}_A = \sum_{a,a'} \rho_{a,a'} |a\rangle \langle a'|, \quad \hat{\rho}_B = \sum_{b,b'} \rho_{b,b'} |b\rangle \langle b'|, \quad (2.17)$$

the density operators in sub-systems A and B , respectively.

2.1.4 Thermal-equilibrium density operators

The classical density-distribution function for an statistical ensemble has a correspondence with the density operator when we compute the average of observables. Therefore, as expected, the density operator $\hat{\rho}$ could represent statistical ensembles [Greiner et al., 2012, Nolting et al., 2018].

The evolution of an observable $\langle \hat{\mathcal{A}} \rangle$, based on the definition in Eq. (2.7) and Liouville's equation (2.8), is given by

$$\frac{d}{dt} \langle \hat{\mathcal{A}} \rangle = -i \langle [\hat{\mathcal{H}}, \hat{\mathcal{A}}] \rangle. \quad (2.18)$$

No matter the form of $\hat{\mathcal{A}}$, for obtaining an stationary ensemble, it is, where the average observables does not evolve, is necessary

$$\frac{d}{dt} \langle \hat{\mathcal{A}} \rangle = 0 \longrightarrow [\hat{\mathcal{H}}, \hat{\rho}] = 0, \quad (2.19)$$

which imposes that $\hat{\rho}$ commute with $\hat{\mathcal{H}}$. The restriction in Eq. (2.19) could be satisfied when the density operator $\hat{\rho} = \hat{\rho}(\hat{\mathcal{H}})$ is a function of $\hat{\mathcal{H}}$, which happens for the following ensembles.

Canonical density operator

For a system at fixed temperature T , volume V and number of particle N , the canonical ensemble describes the system through the density operator

$$\hat{\rho}_{\text{Can}} = \frac{e^{-\beta \hat{\mathcal{H}}}}{Z}, \quad Z = \text{Tr}[e^{-\beta \hat{\mathcal{H}}}], \quad (2.20)$$

where $\beta = (k_B T)^{-1}$ with k_B the Boltzmann constant, and Z is the canonical partition function. This definition ensures the condition of stationary ensemble in Eq. (2.19).

Grand-canonical density operator

For a system at fixed temperature T , volume V and chemical potential μ , the grand-canonical ensemble describes the system through density operator

$$\hat{\rho}_{\text{GCan}} = \frac{e^{-\beta(\hat{\mathcal{H}}-\mu\hat{N})}}{\mathcal{Z}}, \quad \mathcal{Z} = \text{Tr}[e^{-\beta(\hat{\mathcal{H}}-\mu\hat{N})}], \quad (2.21)$$

where \hat{N} is the number operator and \mathcal{Z} is the grand-canonical partition function. This definition ensures the condition of stationary ensemble in Eq. (2.19).

2.2 Model nanojunction

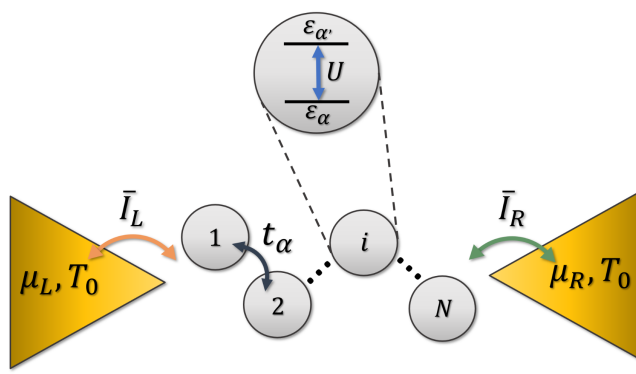


Figure 2.2: Model of nanojunction where a nano-sized material is placed between two leads. The nano-sized material is modelled as a conducting array based on N sites connected between them by a hopping rate t_α between the local energy levels ε_α , and Coulomb interaction U appears for electrons at the same site. When a bias voltage is applied, the split of the lead chemical potentials, μ_L and μ_R , induces stationary electron currents at the left and right contacts, \bar{I}_L and \bar{I}_R .

The modelled nanojunction, shown in Fig. 2.2, is described by the Hamiltonian

$$\hat{\mathcal{H}} = \hat{\mathcal{H}}_C + \hat{\mathcal{H}}_E + \hat{\mathcal{H}}_I, \quad (2.22)$$

where the nano-sized material described by $\hat{\mathcal{H}}_C$, interacts with an environment described by $\hat{\mathcal{H}}_E$, through a interaction Hamiltonian $\hat{\mathcal{H}}_I$. Because of the nano-sized material and the environment are composed by many-particles systems, an easy and compact way for describing them is use the second quantization theory, where the Hamiltonians are written in terms creation and annihilation operators [Bruus and Flensberg, 2004, Mahan, 2013].

2.2.1 Second quantization theory

Any N -particle system could be described in Fock space using the number eigenstates

$$|n_1, n_2, \dots\rangle, \quad \sum_\alpha n_\alpha = N, \quad (2.23)$$

where the number n_α in the Fock state represents the number of particles in the state (orbital) ϕ_α of the system, while the right condition ensures the system contains N particles. The Fock states $\{|n_1, n_2, \dots\rangle\}$ define an orthonormal basis, i.e.,

$$\langle n_1, n_2, \dots | n'_1, n'_2, \dots \rangle = \delta_{n_1, n'_1} \delta_{n_2, n'_2} \dots, \quad (2.24)$$

where δ is a Kronecker delta.

In second quantization \hat{n}_α is the local number operator of particles in the state ϕ_α , of which a Fock state in an eigenstate, i.e.

$$\hat{n}_\alpha |..., n_{\alpha-1}, n_\alpha, n_{\alpha+1}... \rangle = n_\alpha |..., n_{\alpha-1}, n_\alpha, n_{\alpha+1}... \rangle, \quad (2.25)$$

where n_α is the eigenvalue. Based on the local number operators in Eq. (2.25), the total number operator is given by

$$\hat{\mathcal{N}} = \sum_\alpha \hat{n}_\alpha. \quad (2.26)$$

Bosons

For bosons, the number of particles per state, $n_\alpha = \{0, 1, 2, \dots\}$, is restricted to non-negative numbers, while the local number operator is defined as $\hat{n}_\alpha = \hat{a}_\alpha^\dagger \hat{a}_\alpha$, where the operators \hat{a}_α and \hat{a}_α^\dagger annihilates and creates, respectively, a boson in the state α , according to

$$\begin{aligned} \hat{a}_\alpha |..., n_{\alpha-1}, n_\alpha, n_{\alpha+1}... \rangle &= \sqrt{n_\alpha} |..., n_{\alpha-1}, n_\alpha - 1, n_{\alpha+1}, ... \rangle, \\ \hat{a}_\alpha^\dagger |..., n_{\alpha-1}, n_\alpha, n_{\alpha+1}, ... \rangle &= \sqrt{n_\alpha + 1} |..., n_{\alpha-1}, n_\alpha + 1, n_{\alpha+1}, ... \rangle, \end{aligned} \quad (2.27)$$

which, because of the symmetry permutation of the boson-wave function, respects the commutation rules

$$[\hat{a}_\alpha, \hat{a}_\beta] = 0, \quad [\hat{a}_\alpha^\dagger, \hat{a}_\beta^\dagger] = 0, \quad [\hat{a}_\alpha, \hat{a}_\beta^\dagger] = \delta_{\alpha,\beta}, \quad (2.28)$$

Fermions

For Fermions, the number of particles per state, $n_\alpha = \{0, 1\}$, is restricted to that two values, while the local number operator is defined as $\hat{n}_\alpha = \hat{c}_\alpha^\dagger \hat{c}_\alpha$, where the operators \hat{c}_α and \hat{c}_α^\dagger annihilates and creates, respectively, a fermion in the state α , according to

$$\begin{aligned} \hat{c}_\alpha |..., n_{\alpha-1}, 0_\alpha, n_{\alpha+1}, ... \rangle &= 0 = \hat{c}_\alpha^\dagger |..., n_{\alpha-1}, 1_\alpha, n_{\alpha+1}, ... \rangle, \\ \hat{c}_\alpha |..., n_{\alpha-1}, 1_\alpha, n_{\alpha+1}, ... \rangle &= |..., n_{\alpha-1}, 0_\alpha, n_{\alpha+1}, ... \rangle, \\ \hat{c}_\alpha^\dagger |..., n_{\alpha-1}, 0_\alpha, n_{\alpha+1}, ... \rangle &= |..., n_{\alpha-1}, 1_\alpha, n_{\alpha+1}, ... \rangle, \end{aligned} \quad (2.29)$$

which, because of the anti-symmetry permutation in the fermion-wave function, respects the anti-commutation rules

$$\{\hat{c}_\alpha, \hat{c}_\beta\} = 0, \quad \{\hat{c}_\alpha^\dagger, \hat{c}_\beta^\dagger\} = 0, \quad \{\hat{c}_\alpha, \hat{c}_\beta^\dagger\} = \delta_{\alpha,\beta}, \quad (2.30)$$

where $\{\hat{c}_\alpha, \hat{c}_\beta\} = \hat{c}_\alpha \hat{c}_\beta + \hat{c}_\beta \hat{c}_\alpha$ is the anticommutator.

Operators

In a N -particle system, a one-particle operator $\hat{\mathcal{O}}_1$ and a two-particle operator $\hat{\mathcal{O}}_2$ have a form

$$\hat{\mathcal{O}}_1 = \sum_{s=1}^N \hat{T}_s, \quad \hat{\mathcal{O}}_2 = \sum_{s \neq s'}^N \hat{V}_{s,s'}, \quad (2.31)$$

where the operator $\hat{T}_s \equiv T(\vec{r}_s)$ acts over the particle s at position \vec{r}_s , while the operator $\hat{V}_{s,s'} \equiv V(\vec{r}_s, \vec{r}_{s'})$ acts over the particle s and s' at positions \vec{r}_s and $\vec{r}_{s'}$, respectively.

In second quantization, the operators in Eq. (2.31) could be written as

$$\begin{aligned}\hat{O}_1 &= \sum_{\alpha,\alpha'} T_{\alpha\alpha'} \hat{u}_\alpha^\dagger \hat{u}_{\alpha'}, \quad T_{\alpha\alpha'} = \int \phi_\alpha^*(\vec{r}) T(\vec{r}) \phi_{\alpha'}(\vec{r}) d\vec{r}, \\ \hat{O}_2 &= \sum_{\alpha,\alpha',\beta,\beta'} V_{\alpha\alpha',\beta\beta'} \hat{u}_\alpha^\dagger \hat{u}_{\alpha'}^\dagger \hat{u}_\beta \hat{u}_{\beta'}, \quad V_{\alpha\alpha',\beta\beta'} = \int \phi_\alpha^*(\vec{r}) \phi_{\alpha'}^*(\vec{r}) V(\vec{r}, \vec{r}') \phi_\beta(\vec{r}) \phi_{\beta'}(\vec{r}') d\vec{r} d\vec{r}',\end{aligned}\quad (2.32)$$

where \hat{u}_α^\dagger and \hat{u}_α are the creation and annihilation operators, respectively, of either fermions or bosons at the state ϕ_α .

2.2.2 Conducting array

The nano-sized material, either quantum dots or single molecules, attached to the leads is modelled as a conducting array of N sites and α local energy levels per site, as shown in Fig. 2.2. An isolated electron in site i and local energy level α is described by the atomic-like orbital wave function $\phi_{i,\alpha}$ and has a (local) energy ε_α^i . For a system of S interacting electrons with equal mass m_e and charge e in the conducting array, the Hamiltonian is

$$\hat{\mathcal{H}}_C = \sum_{s \in S} \left(\frac{\vec{p}_s^2}{2m_e} + V(\vec{r}_s) \right) + \frac{1}{2} \sum_{s \neq s' \in S} \frac{e^2}{|\vec{r}_s - \vec{r}_{s'}|}, \quad (2.33)$$

where the first summation correspond to the kinetic energy and the ion-core potential of an isolated electron s , and the second summation corresponds to the Coulomb repulsion between electrons s and s' .

The conducting array Hamiltonian in Eq. (2.33) in second quantization, is described by fermionic creation and annihilation operators, $\hat{c}_{i,\alpha}^\dagger$ and $\hat{c}_{i,\alpha}$, respectively, for electrons in site i and orbital $\phi_{i,\alpha}$ in the form [Hubbard, 1963, Hubbard, 1967]¹

$$\hat{\mathcal{H}}_C = \sum_{i,j} \sum_{\alpha,\alpha'} T_{\alpha\alpha'}^{ij} \hat{c}_{i,\alpha}^\dagger \hat{c}_{j,\alpha'} + \frac{1}{2} \sum_{i,j,k,l} \sum_{\alpha,\alpha',\beta,\beta'} I_{ijkl}^{\alpha\alpha',\beta\beta'} \hat{c}_{i,\alpha}^\dagger \hat{c}_{j,\alpha'}^\dagger \hat{c}_{l,\beta} \hat{c}_{k,\beta'}, \quad (2.34)$$

where

$$\begin{aligned}T_{\alpha\alpha'}^{ij} &= \int \phi_{i,\alpha}^*(\vec{r}) \left(\frac{\vec{p}^2}{2m_e} + V(\vec{r}) \right) \phi_{j,\alpha'}(\vec{r}) d\vec{r}, \\ I_{\alpha\alpha',\beta\beta'}^{ijkl} &= \int \phi_{i,\alpha}^*(\vec{r}) \phi_{j,\alpha'}^*(\vec{r}) \left(\frac{e^2}{|\vec{r} - \vec{r}'|} \right) \phi_{k,\beta}(\vec{r}) \phi_{l,\beta'}(\vec{r}') d\vec{r} d\vec{r}',\end{aligned}\quad (2.35)$$

¹In the following, the spin degree of freedom of electron is not considered, but it could be taken into account by adding an index $\sigma = \{\downarrow, \uparrow\}$ in the fermionic operators.

are the hopping and the coulomb interaction integrals, respectively. The hopping and the coulomb integrals in Eq. (2.35) can be approximated to

$$\begin{aligned} T_{\alpha\alpha}^{ij} &= \varepsilon_\alpha^i \delta_{\alpha,\alpha} \delta_{i,j} + t_\alpha^{i,j} \delta_{\alpha,\alpha} (\delta_{j,i+1} + \delta_{i,j+1}), \\ I_{\alpha\alpha,\beta\beta}^{ijkl} &= U_{\alpha,\alpha}^i \delta_{j,i} \delta_{l,i} \delta_{k,j} \delta_{\beta,\alpha} \delta_{\beta,\alpha}, \end{aligned} \quad (2.36)$$

where the hopping integral describes the local energy ε_α^i and electron hopping between the site i and $i+1$ in the local level ϕ_α at rate $t_\alpha^{i,i+1}$, while the coulomb integral describes repulsion between electrons in the same site i at different local levels ϕ_α and ϕ_α , with energy $U_{\alpha,\alpha}^i$. Using the approximation in Eq.(2.36), the conducting array Hamiltonian in Eq. (2.34) is reduced to

$$\hat{\mathcal{H}}_C = \sum_i \left(\sum_\alpha \varepsilon_\alpha \hat{c}_{i,\alpha}^\dagger \hat{c}_{i,\alpha} + \frac{U}{2} \sum_{\alpha \neq \alpha} \hat{c}_{i,\alpha}^\dagger \hat{c}_{i,\alpha} \hat{c}_{i,\alpha}^\dagger \hat{c}_{i,\alpha} + \sum_\alpha t_\alpha (\hat{c}_{i,\alpha}^\dagger \hat{c}_{i+1,\alpha} + \hat{c}_{i+1,\alpha}^\dagger \hat{c}_{i,\alpha}) \right), \quad (2.37)$$

where was considered equals local energies, $\varepsilon_\alpha^i \equiv \varepsilon_\alpha$, Coulomb energies, $U_{\alpha,\alpha}^i \equiv U$, and hopping rates, $t_\alpha^{i,i+1} \equiv t_\alpha$. In the case of circular conducting array, the overlap between the site $i = 1$ and the site $i = N$ produces a non-zero hopping constant t_α between these sites, subject to the periodic boundary condition $N + 1 = 1$.

The conducting array Hamiltonian in Eq. (2.37) could be written in diagonal form as

$$\hat{\mathcal{H}}_C = \sum_n \omega_n |e_n\rangle \langle e_n| \quad (2.38)$$

where $\{\omega_n\}$ is the conducting array spectrum and $\{|e_n\rangle\}$ are the array eigenstates. In the case of N sites and α local energy levels, the number of eigenstates will be $2^{N \times \alpha}$, which increases exponentially. Is expected the hopping rate t_α produces eigenstates which looks as a linear combination of electrons at different sites of the conducting array (delocalization), which induces the conducting array to behave as a large single site [Yoffe, 2001].

Despite the approximation done for the conducting array Hamiltonian in Eq. (2.37), in principle other approximations could be done, because of the nanojunction dynamics (discussed in Chapter 3) considers the array Hamiltonian in diagonal form as Eq. (2.38), which ensures that internal interactions are taken into account [Pedersen and Wacker, 2005, Esposito and Galperin, 2009].

2.2.3 Environment

The environment is composed by different reservoirs: the leads ($\{L, R\}$), the radiation (rad) and thermalized phonons (ph), described generically as a sum of individual Hamiltonian $\hat{\mathcal{H}}_\lambda$,

$$\hat{\mathcal{H}}_E = \sum_{\lambda=\{L,R,\text{rad},\text{ph}\}} \hat{\mathcal{H}}_\lambda. \quad (2.39)$$

of the reservoir λ . In thermal equilibrium, the reservoirs are described by the thermal density operators discussed in Sec. 2.1.4.

Leads

Considering a lead $l = \{L, R\}$ as an electron-gas reservoir, it means free electrons, with well defined temperature T , volume V and chemical potential μ_l , the Hamiltonian is

$$\hat{\mathcal{H}}_l = \sum_s \frac{\vec{p}_s^2}{2m_e}, \quad (2.40)$$

with eigenfunctions and energies

$$\phi_{\vec{k}}(\vec{r}) = \frac{1}{\sqrt{V}} e^{i\vec{k} \cdot \vec{r}}, \quad \omega_{\vec{k}} = \frac{\vec{k}^2}{2m_e}, \quad (2.41)$$

respectively. In the second quantization theory, the lead Hamiltonian in Eq. (2.40), using the Eq. (2.32) and Eq. (2.41), becomes

$$\hat{\mathcal{H}}_l = \sum_{\vec{k}} \omega_{\vec{k}} \hat{c}_{l,\vec{k}}^\dagger \hat{c}_{l,\vec{k}}, \quad (2.42)$$

where $\hat{c}_{l,\vec{k}}$ ($\hat{c}_{l,\vec{k}}^\dagger$) annihilates (creates) one electron in the lead l in the mode \vec{k} .

The grand-canonical density operator and Hamiltonian for the leads are given by

$$\hat{\rho}_l = \frac{\exp(-\beta_0(\hat{\mathcal{H}}_l - \mu_l \hat{\mathcal{N}}_l))}{\text{Tr}_l \left[\exp(-\beta_0(\hat{\mathcal{H}}_l - \mu_l \hat{\mathcal{N}}_l)) \right]}, \quad \hat{\mathcal{H}}_l = \sum_k \omega_k \hat{c}_{l,k}^\dagger \hat{c}_{l,k}, \quad \hat{\mathcal{N}}_l = \sum_k \hat{c}_{l,k}^\dagger \hat{c}_{l,k}, \quad (2.43)$$

where $\beta_0 = (k_B T_0)^{-1}$ at temperature T_0 , μ_l the chemical potential, $\hat{\mathcal{H}}_l$ the number operator and Tr_l is the trace over the degrees of freedom of the lead l .

Radiation

Maxwell's equations describe radiation in free space by the electric field \vec{E} and the magnetic field \vec{B} . In the Coulomb gauge, both fields are computed through the vector potential \vec{A} as

$$\vec{E} = -\frac{1}{c} \frac{\partial \vec{A}}{\partial t}, \quad \vec{B} = \vec{\nabla} \times \vec{A}, \quad (2.44)$$

where c is the speed of light.

Considering radiation in homogeneous space with lineal polarization $\vec{\epsilon}_k$ in a volume V , the vector potential is reduced to [Nitzan, 2006]

$$\hat{\vec{A}} = c \sum_{\vec{k}} \sqrt{\frac{2\pi}{\epsilon_0 V \omega_{\vec{k}}}} \left(\hat{a}_{\text{rad},\vec{k}} \exp(i(\vec{k} \cdot \vec{r} - \omega_{\vec{k}} t)) + \hat{a}_{\text{rad},\vec{k}}^\dagger \exp(-i(\vec{k} \cdot \vec{r} - \omega_{\vec{k}} t)) \right) \vec{\epsilon}_k, \quad (2.45)$$

where ϵ_0 is the permittivity of free space, and $\hat{a}_{\text{rad},\vec{k}}$ and $\hat{a}_{\text{rad},\vec{k}}^\dagger$ are bosonic creation and annihilation operators, respectively, of photons in the mode \vec{k} . Based on the fields defined in Eq. (2.44) and

the potential vector in Eq. (2.45), the energy of radiation is given by

$$\hat{\mathcal{H}}_{\text{rad}} = \sum_{\vec{k}} \omega_{\vec{k}} \left(\hat{a}_{\text{rad},\vec{k}}^\dagger \hat{a}_{\text{rad},\vec{k}} + \frac{1}{2} \right), \quad (2.46)$$

where $\omega_{\vec{k}}$ is the energy of the mode \vec{k} .

The canonical-density operator and Hamiltonian for radiation are given by

$$\hat{\rho}_{\text{rad}} = \frac{\exp(-\beta_0 \hat{\mathcal{H}}_{\text{rad}})}{\text{Tr}_{\text{rad}} [\exp(-\beta_0 \hat{\mathcal{H}}_{\text{rad}})]}, \quad \hat{\mathcal{H}}_{\text{rad}} = \sum_p \omega_p \hat{a}_{\text{rad},p}^\dagger \hat{a}_{\text{rad},p}, \quad (2.47)$$

where Tr_{rad} is the trace over the degrees of freedom of radiation.

Phonons

Considering a group of N atomic-ion cores with equal mass m_N at the site of the conducting array. If they are connected by a elastic constant K , they are be described by the Hamiltonian [Scheer and Cuevas, 2017]

$$\hat{\mathcal{H}}_{\text{ph}} = \sum_i \frac{P_i^2}{2m_N} + \frac{K}{2} \sum_i (R_i - R_{i-1})^2, \quad (2.48)$$

where P_i and R_i are the momentum and the position of the i -th atomic-ion core. Applying a Fourier transform, the canonical variables R_i and P_i becomes

$$R_k = \frac{1}{\sqrt{N}} \sum_j R_j \exp(-ikaj), \quad P_k = \frac{1}{\sqrt{N}} \sum_j P_j \exp(ikaj), \quad (2.49)$$

where a is the distance between cores and the commutation relation $[R_k, P_k] = i\delta_{k,k}$ is preserved also in the k -space.

Based on the Fourier transform in Eq. (2.49), the phonon Hamiltonian in Eq. (2.48) could be written as

$$\hat{\mathcal{H}}_{\text{ph}} = \sum_k \frac{1}{2m_N} P_k P_{-k} + \sum_k \frac{m_N \omega_k}{2} R_k R_{-k}, \quad \omega_k = \frac{4K}{m_N} \sin^2 \left(\frac{ka}{2} \right), \quad (2.50)$$

where ω_k is the energy in the mode k . Defining

$$\hat{a}_{\text{ph},k} = \sqrt{\frac{m_N \omega_k}{2}} \left(R_k + \frac{i}{m_N \omega_k} P_{-k} \right), \quad \hat{a}_{\text{ph},k}^\dagger = \sqrt{\frac{m_N \omega_k}{2}} \left(R_{-k} - \frac{i}{m_N \omega_k} P_k \right), \quad (2.51)$$

the creation and annihilation operators, respectively, of phonon in the mode k , the phonon Hamiltonian in Eq. (2.50) could be easily written in the second quantization theory as

$$\hat{\mathcal{H}}_{\text{ph}} = \sum_k \omega_k \left(\hat{a}_{\text{ph},k}^\dagger \hat{a}_{\text{ph},k} + \frac{1}{2} \right). \quad (2.52)$$

The canonical-density operator and Hamiltonian for atomic-ion cores are given by,

$$\hat{\rho}_{\text{ph}} = \frac{\exp(-\beta_0 \hat{\mathcal{H}}_{\text{ph}})}{\text{Tr}_{\text{ph}} [\exp(-\beta_0 \hat{\mathcal{H}}_{\text{ph}})]}, \quad \hat{\mathcal{H}}_{\text{ph}} = \sum_q \omega_q \hat{a}_{\text{ph},q}^\dagger \hat{a}_{\text{ph},q}, \quad (2.53)$$

where Tr_{ph} is the trace over the degrees of freedom of the phonons ph.

2.2.4 Interactions

All the reservoirs interact with the conducting array, defining a total interaction,

$$\hat{\mathcal{H}}_I = \sum_{\lambda=\{L,R,\text{rad},\text{ph}\}} \hat{\mathcal{H}}_I^\lambda, \quad (2.54)$$

as a sum of individual system-reservoir interaction $\hat{\mathcal{H}}_I^\lambda$ of the reservoir λ and the conducting array. Through the interactions, the thermodynamic parameters of the reservoirs induces non-equilibrium dynamics in the conducting array.

Lead tunneling

When the lead $l = \{L, R\}$ is next to the conducting array, the overlapping of the electronic wave functions produce electron transfer between them, described by the Hamiltonian

$$\hat{\mathcal{H}}_I^l = \sum_{i,\alpha,k} \left(V_{il}^{\alpha k} \hat{c}_{i,\alpha}^\dagger \hat{c}_{l,k} + (V_{il}^{\alpha k})^* \hat{c}_{l,k}^\dagger \hat{c}_{i,\alpha} \right), \quad (2.55)$$

as a tunneling process [Scheer and Cuevas, 2017]. $V_{il}^{\alpha k}$ is the coupling constant between an electron in the lead l in the mode k and an electron in the conducting array site i and local energy level α . We ignores energy (exciton) transfer with the leads, which is an operator of fourth order in fermion operators and acts as a non-radiative de-excitation of the conducting array through the creation of a electron-hole pair in the leads [Galperin and Nitzan, 2005, Galperin and Nitzan, 2006]. We assume that the coupling constant,

$$V_{il}^{\alpha k} = u_i^{(l)} V_k^{(l)}, \quad (2.56)$$

could be divided in a conducting array term, $u_i^{(l)} \in \mathbb{R}$, and a reservoir part, $V_k^{(l)} \in \mathbb{C}$.

With the coupling approximation in Eq. (2.56), the interaction Hamiltonian in Eq. (2.55) becomes

$$\hat{\mathcal{H}}_I^l = \sum_{i,\alpha,k} u_i^{(l)} \left(V_k^{(l)} \hat{c}_{i,\alpha}^\dagger \hat{c}_{l,k} + V_k^{(l)*} \hat{c}_{l,k}^\dagger \hat{c}_{i,\alpha} \right), \quad (2.57)$$

where we modelled the conducting array dependence, $u_i^{(l)}$, as a Kronecker delta function whit value 1 when the conducting array site i is the nearest site to the lead l , because it is where the coupling is highest.

Light-matter interaction

The interaction between the radiation and the conducting array, up to the dipolar approximation, is given by [Nitzan, 2006]

$$\hat{\mathcal{H}}_I^{\text{rad}} = - \sum_s \hat{\vec{\mu}}_s \cdot \hat{\vec{E}}(\vec{r}_s), \quad (2.58)$$

where $\hat{\vec{\mu}}_s$ is the dipole operator of an electron s of the conducting array and $\hat{\vec{E}}(\vec{r}_s)$ is the electric field in the Schrödinger picture at the position \vec{r}_s of an electron s . Considering the radiation wavelength greater than the conducting array length, the electric field $\hat{\vec{E}}(\vec{r} = 0)$ is spatially constant, defining $\vec{r} = 0$ at the beginning of the conducting array.

In second quantization, applying the Eq. (2.32), the dipole operator could be written as,

$$\sum_s \hat{\vec{\mu}}_s = \sum_i \sum_{\alpha \neq \alpha'} \bar{\mu}_i^{\alpha\alpha'} \hat{c}_{i,\alpha}^\dagger \hat{c}_{i,\alpha'}, \quad \bar{\mu}_i^{\alpha\alpha'} = \int \phi_{i,\alpha}^*(\vec{r}) \hat{\vec{\mu}}(\vec{r}) \phi_{i,\alpha'}(\vec{r}) d\vec{r}, \quad (2.59)$$

where $\bar{\mu}_i^{\alpha\alpha'}$ is the dipole integral. In Eq. (2.59) we have considered only dipole transitions between the different levels at the same site, ignoring excimer formation² and permanent dipole moments. Considering the dipole operator in Eq. (2.59) and the electric field defined in Eq. (2.44), the interaction Hamiltonian in Eq. (2.58), under the rotating-wave approximation (RWA), becomes,

$$\hat{\mathcal{H}}_I^{\text{rad}} = \sum_{i,\alpha > \alpha', p} u_i^{(\text{rad})} \left(V_p^{(\text{rad})} \hat{c}_{i,\alpha}^\dagger \hat{c}_{i,\alpha'} \hat{a}_{\text{rad},p} + V_p^{(\text{rad})*} \hat{c}_{i,\alpha'}^\dagger \hat{c}_{i,\alpha} \hat{a}_{\text{rad},p}^\dagger \right), \quad (2.60)$$

where we has assumed the dipole operator is aligned with the electric field polarization and the coupling constant

$$u_i^{(\text{rad})} V_p^{(\text{rad})} = -i \sqrt{\frac{2\pi\omega_p}{\epsilon_0 V}} \bar{\mu}_i^{\alpha\alpha'}. \quad (2.61)$$

This could be divided into a conducting array term, $u_i^{(\text{rad})} \in \mathbb{R}$, and a reservoir part, $V_p^{(\text{rad})} \in \mathbb{C}$. We model the conducting array dependence, $u_i^{(\text{rad})} = 1$, as a constant value for all the conducting array sites, because are considered the dipoles operators equals for all the conducting array sites.

Electron-phonon interaction

The interaction between electrons in the conducting array and the atomic-ion cores is described by the Hamiltonian

$$\hat{\mathcal{H}}_I^{\text{ph}} = \sum_{s,i} V(r_s - R_i), \quad (2.62)$$

where $V(r_s - R_i)$ is a potential of an electron s and an atomic-ion core i . Expanding the potential respect to the equilibrium position R_i^0 of the atomic-ion cores, up to first order in the Taylor expansion the Hamiltonian interaction in Eq. (2.62) becomes [Mahan, 2013]

$$\begin{aligned} \hat{\mathcal{H}}_I^{\text{ph}} &= - \sum_{s,i} Q_i \frac{\partial}{\partial R_i} V(r_s - R_i) |_{R_i=R_i^0}, \\ Q_i &= R_i - R_i^0 = \frac{1}{\sqrt{N}} \sum_q \sqrt{\frac{1}{2m_N\omega_q}} \left(\hat{a}_{\text{ph},q} + \hat{a}_{\text{ph},-q}^\dagger \right) \exp(iqR_i^0), \end{aligned} \quad (2.63)$$

²Electron transfer between different conducting array sites.

where Q_i is the displacement operator in terms of phonon creation and annihilation operator defined in Eq. (2.51).

Writing the potential $V(r_s - R_n)$ in Fourier transform space,

$$V(r_s - R_i) = \frac{1}{\sqrt{N}} \sum_q V_q \exp(iq(r_s - R_i)), \quad (2.64)$$

the Hamiltonian in Eq. (2.63) reduces to

$$\hat{\mathcal{H}}_I^{\text{ph}} = \sum_{s,q} g_{s,q} \left(\hat{a}_{\text{ph},q} + \hat{a}_{\text{ph},-q}^\dagger \right), \quad g_{s,q} = i \sqrt{\frac{1}{2m_N \omega_q}} q V_q \exp(iqr_s), \quad (2.65)$$

where $g_{s,q}$ is a one-electron operator, which, written in second quantization theory using Eq. (2.32), becomes

$$\sum_s g_{s,q} = \sum_i \sum_\alpha u_i^{(\text{ph})} V_q^{(\text{ph})} \hat{c}_{i,\alpha}^\dagger \hat{c}_{i,\alpha}, \quad u_i^{(\text{ph})} V_q^{(\text{ph})} = \int \phi_{i,\alpha}^*(\vec{r}) g_q \phi_{i,\alpha}(\vec{r}) d\vec{r}, \quad (2.66)$$

where it has been assumed that the integral gives a non-zero coupling constant, $u_i^{(\text{ph})} V_q^{(\text{ph})}$, only for electron in the same site and energy level [Gauger et al., 2008].

With the coupling constant approximation in Eq. (2.66), the Hamiltonian interaction in Eq. (2.65) is reduced to

$$\hat{\mathcal{H}}_I^{\text{ph}} = \sum_{i,\alpha,q} u_i^{(\text{ph})} V_q^{(\text{ph})} \hat{c}_{i,\alpha}^\dagger \hat{c}_{i,\alpha} \left(\hat{a}_{\text{ph},q} + \hat{a}_{\text{ph},q}^\dagger \right), \quad (2.67)$$

where we model the conducting array dependence as $u_i^{(\text{ph})} = (-1)^{i+1}$, because it takes into account a relative π -phase between conducting array sites [Sowa et al., 2017].

Chapter 3

Nanojunction dynamics

Many theoretical methods have been developed for treating the dynamics of non-equilibrium systems such as the nanojunctions described in Sec. 2.2. Considering the non-equilibrium system as an open-quantum system, the density operator formalism, discussed in Sec. 2.1, can be used to derive a quantum master equation for the system dynamics under a set of approximations and assumptions. Although quantum master equations do not provide exact dynamics, they have been applied to chemical and physical problems due to its intuitive results and easy implementation. This Chapter discusses the nanojunction dynamics through a quantum master equation, which captures the interaction of a conducting array with the environment as transition between conducting array eigenstates induced by the individual reservoirs. Based on the nanojunction dynamics, we derive an expression for the electron current through the molecule, and the implementation for obtaining the typical current-voltage curve for characterizing the electron transport in nanojunctions is discussed.

3.1 Quantum master equation

The model considers the nanojunction as an open-quantum system, where the conducting array is a quantum system that interacts with an environment composed by different reservoirs, as shown in Fig. 3.1(a). The nanojunction is described by the total density operator $\hat{\rho}$, containing information about the conducting array, through the reduced density operator $\hat{\rho}_C = \text{Tr}_E [\hat{\rho}]$, and the environment, through the reduced density operator $\hat{\rho}_E = \text{Tr}_C [\hat{\rho}]$.

Considering weak system-reservoir coupling, the interaction Hamiltonian $\hat{\mathcal{H}}_I$ is considered in perturbation theory for the nanojunction dynamics. It means that the environment and conducting array evolve as uncorrelated sub-systems. Considering also that the environment is bigger than the conducting array (Born approximation), the total density operator is

$$\hat{\rho}(t) = \hat{\rho}_C(t) \otimes \hat{\rho}_E, \quad (3.1)$$

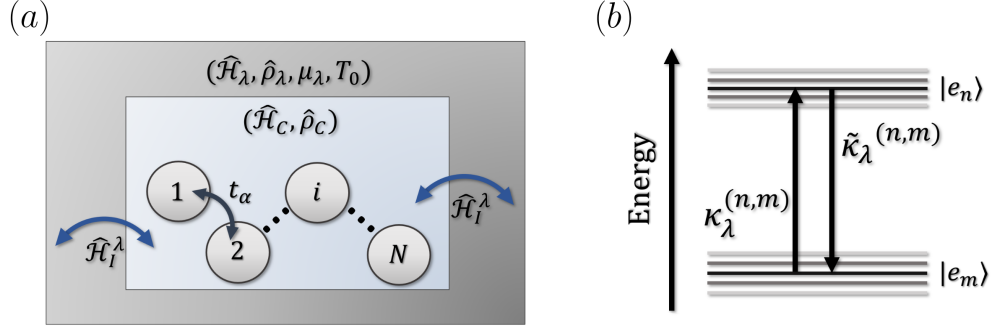


Figure 3.1: (a) Open-quantum system picture, where the conducting array, described by $(\hat{\mathcal{H}}_C, \hat{\rho}_C)$, interact with a reservoir λ , described by $(\hat{\mathcal{H}}_\lambda, \hat{\rho}_\lambda, \mu_\lambda, T_0)$, through an interaction Hamiltonian $\hat{\mathcal{H}}_I^\lambda$. (b) Diagram of electron transitions induced by a reservoir λ at effective transfer rate $\kappa_\lambda^{(n,m)}$ for $|e_m\rangle \rightarrow |e_n\rangle$ eigenstate transition and effective transfer rate $\tilde{\kappa}_\lambda^{(n,m)}$ for $|e_n\rangle \rightarrow |e_m\rangle$ eigenstate transition.

i.e. looks as a tensor product of the conducting array density operator, $\hat{\rho}_C(t)$, which evolves as a function of time, and the environment density operator,

$$\hat{\rho}_E = \hat{\rho}_L \otimes \hat{\rho}_R \otimes \hat{\rho}_{\text{rad}} \otimes \hat{\rho}_{\text{ph}}, \quad (3.2)$$

which is composed by thermal density operators for all the reservoirs, as discussed in Sec. 2.2.3. The Liouville equation for the total density operator $\hat{\rho}$ in Eq. (2.8) is reduced to the Redfield equation (derivation in Appendix A)

$$\frac{d}{dt} \hat{\rho}_C(t) = -i \left[\hat{\mathcal{H}}_C, \hat{\rho}_C(t) \right] - \int_0^\infty d\tau \text{Tr}_E \left[\hat{\mathcal{H}}_I, \left[\hat{\mathcal{H}}_I(-\tau), \hat{\rho}_C(t) \otimes \hat{\rho}_E \right] \right], \quad (3.3)$$

for the conducting array dynamics, where $\hat{\mathcal{H}}_I(-\tau)$ is the interaction Hamiltonian in the interaction picture at time $-\tau$. It was also considered the Markov approximation, because of the reservoir correlations decay faster on time than the conducting array dynamics and we consider the environment at room temperature [Timm, 2008].

Given the interaction Hamiltonian $\hat{\mathcal{H}}_I$ in Eq. (2.54) and the environment density operators $\hat{\rho}_E$ in Eq. (3.2), the Redfield equation in Eq. (3.3) becomes the a Lindblad quantum master equation (derivation in Appendix B)

$$\frac{d}{dt} \hat{\rho}_C(t) = -i \left[\hat{\mathcal{H}}_C, \hat{\rho}_C(t) \right] + \sum_{n,m} \left(\kappa^{(n,m)} \mathcal{L}_{n,m} [\hat{\rho}_C(t)] + \tilde{\kappa}^{(n,m)} \mathcal{L}_{m,n} [\hat{\rho}_C(t)] \right), \quad (3.4)$$

whit decay rates defined as

$$\kappa^{(n,m)} = \sum_{\lambda=\{L,R,\text{rad},\text{ph}\}} \kappa_\lambda^{(n,m)}, \quad \tilde{\kappa}^{(n,m)} = \sum_{\lambda=\{L,R,\text{rad},\text{ph}\}} \tilde{\kappa}_\lambda^{(n,m)}, \quad (3.5)$$

in terms of the *effective transfer rates* $\kappa_\lambda^{(n,m)}$ and $\tilde{\kappa}_\lambda^{(n,m)}$ (details in Table B.1), and the Lindblad superoperators read

$$\mathcal{L}_{n,m} [\hat{\rho}_C(t)] = \hat{L}_{n,m} \hat{\rho}_C(t) \hat{L}_{n,m}^\dagger - \frac{1}{2} \{ \hat{L}_{n,m}^\dagger \hat{L}_{n,m}, \hat{\rho}_C(t) \}, \quad \hat{L}_{n,m} = |e_n\rangle \langle e_m|, \quad (3.6)$$

which guarantee the positive time evolution of density operator, i.e., the system conserves the probabilities during the evolution [Breuer et al., 2002].

The model describes the open-quantum system dynamics where the conducting array interacts with a reservoir λ as electron transitions are induced by the reservoir at effective transfer rates $\kappa_\lambda^{(n,m)}$ for transition between conducting array eigenstates $|e_m\rangle \rightarrow |e_n\rangle$ and at effective transfer rate $\tilde{\kappa}_\lambda^{(n,m)}$ for transition between conducting array eigenstates $|e_n\rangle \rightarrow |e_m\rangle$, as is shown in Fig. 3.1(b). The transition between eigenstates is related with the addition of subtraction of electrons when it is induced by the leads, unlike when it is induced by radiation or thermalized phonons, which conserves the number of electrons.

The effective transfer rates, $\kappa_\lambda^{(n,m)}$ and $\tilde{\kappa}_\lambda^{(n,m)}$, depend on the conducting array transition frequency $\omega_{n,m} = \omega_n - \omega_m$, and the reservoir thermodynamics parameters, as temperature T_0 and chemical potential μ_λ . The reservoir λ will only induce transition between eigenstates $|e_n\rangle \leftrightarrow |e_m\rangle$ provided that

$$|\langle e_n | \hat{S}_\lambda | e_m \rangle|^2 \neq 0, \quad (3.7)$$

where \hat{S}_λ , defined in Table B.1, is a conducting array operator for a given reservoir λ , which gives the selection rules for reservoir-induced transitions.

Quantum master equations in the Lindblad form has been used for describing the dynamics of nanojunctions [Gurvitz and Prager, 1996, Li et al., 2005, Harbola et al., 2006, Timm, 2008] because its intuitive and simple results when describing weakly coupled systems [Harbola et al., 2006, Esposito and Galperin, 2010, Thoss and Evers, 2018]. Nevertheless, the approximation typically used for deriving them sometimes becomes inadequate and leads to wrong results [Esposito and Galperin, 2010, Ballmann et al., 2012]. Because observables are measured in stationary regime, the Markov approximation, which has been reported reaches the same results that non-Markovian models in the stationary regime [Pedersen and Wacker, 2005], is not the main problem, but the perturbative treatment of coupling with the reservoir, specially at low temperature [Thoss and Evers, 2018]. For example, in single molecules and carbon nanotubes the electronic degree of freedom could be strongly coupled to a specific vibrational mode rather than the vibrational bath [Sowa et al., 2017], or the spin of electrons in quantum dots or single molecules could be strongly correlated to the spins at the leads at low temperature [Kondo, 1964]. That means that interesting transport effects, which requires a non-perturbative treatment for their description, as Franck-Condon blockade or Kondo effect for example, fall outside the scope of our model.

Many methods have been developed to describe nanojunctions in a more exact way. Some of them involves modifications to quantum master equations, which include non-perturbative and non-Markovian effects [Esposito and Galperin, 2009]; taking in to account strong electron-phonon coupling through (small) polaron transformation [Galperin et al., 2006, Galperin and Nitzan, 2006, Esposito and Galperin, 2009, Sowa et al., 2017, Sowa et al., 2018]; higher order perturbation process, through Keldysh formalism [Timm, 2008]; or broadening effects of the molecular levels due

to the coupling with the leads, through non-equilibrium Green functions [Pedersen and Wacker, 2005, Esposito and Galperin, 2009]. For more complex nano-sized material, interesting results have been obtained using *ad-initio* methods, where the equilibrium electronic structure of the conducting material is taken into account through the density of states, mixed with non-equilibrium Green functions [Taylor et al., 2002, Thoss and Evers, 2018].

3.1.1 Rate equations

From the Lindblad quantum master equation in Eq. (3.4), the population $\rho_n \equiv \rho_{n,n} = \langle e_n | \hat{\rho}_C | e_n \rangle$ at the conducting array eigenstate $|e_n\rangle$ evolves according to

$$\frac{d}{dt}\rho_n = \sum_m \left(\kappa^{(n,m)} + \tilde{\kappa}^{(m,n)} \right) \rho_m - \rho_n \sum_m \left(\kappa^{(m,n)} + \tilde{\kappa}^{(n,m)} \right), \quad (3.8)$$

as a system of rate equations, while the coherences $\rho_{i,j} = \langle e_i | \hat{\rho}_C | e_j \rangle$ at the conducting array eigenstates $|e_i\rangle$ and $|e_j\rangle$ evolve according to,

$$\frac{d}{dt}\rho_{i,j} = -i\omega_{i,j}\rho_{i,j} - \frac{1}{2} \sum_m \left(\kappa^{(m,i)} + \kappa^{(m,j)} + \tilde{\kappa}^{(i,m)} + \tilde{\kappa}^{(j,m)} \right) \rho_{i,j}. \quad (3.9)$$

As shown in Eq. (3.8) and (3.9), the dynamics of population and coherences are decoupled when the conducting array dynamics is written in terms of its eigenstates, because we use secular approximation in the derivation [Sowa et al., 2018]. This means that the whole dynamics is reduced to population transfer between conducting array eigenstates with rates according to Fermi golden rules, while the coherences decay to zero in steady state [Kouwenhoven et al., 1997, Esposito and Galperin, 2010]. In principle, the decoupling could not be true if the density operator is written in another basis, for example the local basis [Harbola et al., 2006].

Therefore, for solving the conducting array dynamics in Eq. (3.4), we implement only the population evolutions from the rate equations in Eq. (3.8), because it reduces the system dimension from a full density operator $\hat{\rho}_C$, with $(2^{\alpha \times N})^2$ elements, to populations evolution, with $2^{\alpha \times N}$ elements. Although the model could obtain time dependent observables, for the system characterization the interesting observables are typically measured in the steady state where the set of populations $\{\rho_n\}$ reach stationary values $\{\bar{\rho}_n\}$. Therefore, the rate equations in Eq. (3.8) are solved imposing the stationary conditions, these are,

$$\{\dot{\bar{\rho}}_n\} = 0, \quad \sum_{n=1}^{2^{\alpha \times N}} \bar{\rho}_n = 1. \quad (3.10)$$

where the right condition ensures a non-trivial solution of the system of rates equations when the left condition is satisfied.

3.2 Nanojunction characterization

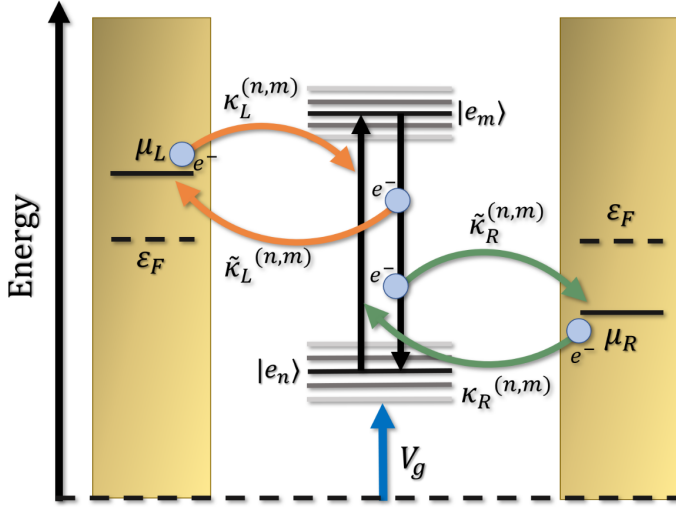


Figure 3.2: Diagram of nanojunction energy levels, where electron transition between conducting array eigenstates are induced by the leads at chemical potentials μ_L and μ_R , splitted respect to the Fermi energy ε_F because an applied positive bias voltage V . The presence of a gate voltage, V_g , induces an electrostatics change of the conducting array levels. Any electron transition is accompanied by an electron addition or subtraction, and the net effect is measured as a current I_L and I_R at the left and right contact, respectively.

Because of the changes of charge number by the electron transitions induced by the leads, as is shown in the Fig. 3.2, a flow (current) of electrons take place at the contact between the conducting array and the leads, even in the steady state. Although the model considers the leads in thermal-equilibrium during all the system dynamics, the non-equilibrium dynamics of the conducting array is associated to an slightly change of the leads observables, as the number of particles, but it is not large enough to change their thermodynamics parameters (equivalent for radiation and thermalized phonon reservoirs).

3.2.1 Current-voltage

With $\hat{\mathcal{N}}_L$ and $\hat{\mathcal{N}}_R$ the number operator of electron at the left and right lead, respectively, the currents at the left and right contacts are defined as (derivation in Appendix C)

$$\begin{aligned} I_L &= -e \frac{d}{dt} \langle \hat{\mathcal{N}}_L \rangle = e \sum_{n,m} \left(\kappa_L^{(n,m)} \rho_m - \tilde{\kappa}_L^{(n,m)} \rho_n \right), \\ I_R &= e \frac{d}{dt} \langle \hat{\mathcal{N}}_R \rangle = -e \sum_{n,m} \left(\kappa_R^{(n,m)} \rho_m - \tilde{\kappa}_R^{(n,m)} \rho_n \right), \end{aligned} \quad (3.11)$$

respectively, which quantifies the variation of electrons in the leads produced by the non-equilibrium conducting array dynamics. The different sign between left and right current is associated to the definition of positive current to right and negative current to left. Giving the set of populations $\{\rho_n\}$ as a function of time, the currents I_L and I_R in Eq. (3.11) could be computed as a function of time too, but for characterizing the system we compute stationary currents \bar{I}_L and \bar{I}_R , based on the set of stationary populations $\{\bar{\rho}_n\}$. Is expected in the steady state $\bar{I}_L = \bar{I}_R$, because of the conservation of electron number.

The contribution of a specific eigenstate $|e_n\rangle$ to the current at the left and right contacts are defined as the *state dependent currents*

$$\begin{aligned} I_L^{(n)} &= e \sum_m \left(\kappa_L^{(n,m)} \rho_m - \tilde{\kappa}_L^{(n,m)} \rho_n \right), \\ I_R^{(n)} &= -e \sum_m \left(\kappa_R^{(n,m)} \rho_m - \tilde{\kappa}_R^{(n,m)} \rho_n \right), \end{aligned} \quad (3.12)$$

respectively. In principle, the state dependent currents could satisfy $\bar{I}_L^{(n)} \neq \bar{I}_R^{(n)}$ in the steady state. However, because of the definition in Eq. (3.11), the sum of all the state dependent currents in their respective contacts must satisfy $\sum_n \bar{I}_L^{(n)} = \sum_n \bar{I}_R^{(n)}$.

An external bias voltage, V , induces a change of the left and right chemical potentials, μ_L and μ_R , respectively, according to the relation

$$\mu_L - \varepsilon_F = \varepsilon_F - \mu_R = \frac{1}{2}eV, \quad (3.13)$$

where the Fermi energy, ε_F , corresponds to the common energy level for the chemical potentials at the zero bias voltage configuration, as is shown in Fig. 3.2 for a case where a positive bias voltage is applied. As expected, if the conducting array allows it, the electrons tend to travel from higher to lower chemical potential, producing a current I_L and I_R in their respective contacts as a function of time, up to a stationary current \bar{I}_L and \bar{I}_R . Therefore, the applied voltage acts as a driving source of electrons through the nanojunction.

In a specific region of voltage where the current modified, gives a peak of (differential) conductance, defined as,

$$\bar{G}_L = \frac{d\bar{I}_L}{dV}, \quad \bar{G}_R = \frac{d\bar{I}_R}{dV}, \quad (3.14)$$

at the left and right contacts, respectively.

3.2.2 Gate voltage

Applying a gate voltage V_g through a third gate induces a change in the conducting energy levels in a continuous manner, as shown in Fig. 3.2. Fixing the empty conducting array eigenstate¹ as the zero-energy reference, when the gate voltage is applied, the induced changes in the nanojunction energy levels are equivalent to a linear decrease of the Fermi energy according to,

$$\varepsilon_F \rightarrow \varepsilon_F - eV_g. \quad (3.15)$$

¹This eigenstate represent the configuration where there is not charge in the conducting array.

Chapter 4

Results

Electron transport through quantum dots and molecular junctions exhibits interesting quantum effects. Understanding these quantum signatures is absolutely necessary for possible applications of these systems as building blocks in nano-electronics.

In this Chapter, we describe the electron transport properties of different nanojunctions in terms of their current-voltage curves, based on the nanojunction description given in Chapter 2 and the dynamics derived in Chapter 3. For a simple conducting array, the electron transition processes induced by different reservoirs are studied. For more complex conducting arrays, state dependent currents and photon fluxes are studied as a function of the conducting array geometry, and the strength of an external source of incoherent light.

In this Chapter, the results have been computed using the parameters in Table 4.1. The rates $\gamma_L, \gamma_R, \gamma_{\text{rad}}$ and γ_{ph} are assumed constant¹. Therefore, the main dependence of the effective transfer rates, $\kappa_{\lambda}^{(n,m)}$ and $\tilde{\kappa}_{\lambda}^{(n,m)}$, comes from the fermion or boson densities, $f_{L(R)}^{(n,m)}$ and $n_{\text{rad(ph)}}^{(n,m)}$, respectively (see details in Table B.2).

Although the rate of spontaneous emission typically has a value of $\gamma_{\text{rad}} \approx 10^{-5}[\text{eV}]$, we analyze the case where it is comparable with the typical tunneling rates ($\gamma_{L(R)} \approx 0.01 - 0, 1[\text{eV}]$), because, when the spontaneous emission rate is slower than tunneling rate, it can be practically ignored, which is not desired when we try to analyse optoelectronic behaviour [Thoss and Evers, 2018]. High spontaneous emission rates, such as those in Table 4.1, have been measured in experiments with plasmonic nanoantennas [Hoang et al., 2015].

¹This approximation is known as the *wide band limit*.

Table 4.1: Nanojunctions parameters, taken from [Harbola et al., 2006, Hoang et al., 2015, Liu and Segal, 2020].

Ground local energy level	ε_g	0.5 eV
Excited local energy level	ε_e	1.5 eV
Hopping rate	t	0.2 eV
Coulomb repulsion energy	U	0.1 eV
Fermi energy	ε_F	0.5 eV
Temperature	T_0	290 K
Left tunneling rate	γ_L	0.01 eV
Right tunneling rate	γ_R	0.01 eV
Spontaneous emission rate	γ_{rad}	0.005 eV
Phonon relaxation rate	γ_{ph}	0.01 eV

4.1 Electron transition processes

In Sec. 3.1 we discuss induced electron transition processes in electron transport. Because different microscopic processes could be present at the same time, for the analysis of one of them, in the following simple conducting arrays are considered.

4.1.1 Resonant tunneling

Consider a conducting array of $N = 1$ site with a local ground energy level ε_g , connected to the leads, as illustrated in Fig. 4.1(a). Based on the parameters in Table 4.1, the nanojunction energy levels are shown in Fig. 4.1(b), for the left lead (L), the conducting array (C) and the right lead (R) at 1[V] bias voltage. The arrows represent transitions between the nanojunction energy levels induced by different reservoirs, each one associated with different colors². In this case, the nanojunction undergoes electron tunneling with the leads, being the simplest conducting array which contains this microscopic process. Tunneling induces population transfer between the conducting array eigenstates $|e_1\rangle = |0_g\rangle$ and $|e_2\rangle = |1_g\rangle$, which represent zero and one electron in the ground local energy level ε_g , respectively.

If the conducting array is initially uncharged, all the population is in the conducting array eigenstate $|e_1\rangle$. The population evolution induced by a applied constant bias voltage of 1[V] is shown in Fig. 4.1(c). The populations evolve up to their stationary values $\bar{\rho}_1$ and $\bar{\rho}_2$ after a time of approximately $10^{-3}[\text{ns}]$, which agree with the typical tunneling time $1/(\gamma_L + \gamma_R) \approx 10^{-3}[\text{ns}]$. As expected, both populations are equal at the steady state because, based on the rates equations in Eq. (3.8), the stationary populations at bias voltage V , given by

$$\bar{\rho}_1 = \frac{\gamma_L \gamma_R}{\gamma_L + \gamma_R} \left(\frac{\tilde{f}_L^{(2,1)}(V)}{\gamma_R} + \frac{\tilde{f}_R^{(2,1)}(V)}{\gamma_L} \right), \text{ and } \bar{\rho}_2 = \frac{\gamma_L \gamma_R}{\gamma_L + \gamma_R} \left(\frac{f_L^{(2,1)}(V)}{\gamma_R} + \frac{f_R^{(2,1)}(V)}{\gamma_L} \right), \quad (4.1)$$

²In the case of tunneling, the arrows only represent the transfer of a single electron between the nanojunction energy levels, but not the induced transitions between the conducting array eigenstates as it was show in Fig. 3.2.

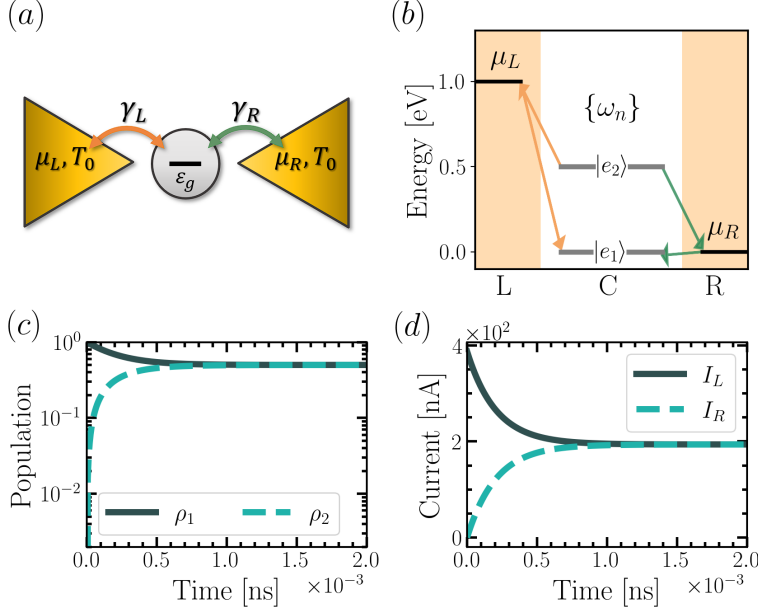


Figure 4.1: For conducting array of $N = 1$ site with a local ground energy level ε_g , connected to the leads; (a) nanojunction; (b) nanojunction energy levels for left lead (L), conducting array (C) and right lead (R) at bias voltage of 1[V], where arrows represent electron transfer induced by left lead (orange) and right lead (green); population (c) and current (d) evolution from conducting array in uncharged configuration when is applied a constant bias voltage of 1[V]. Parameters in Table 4.1.

satisfy $\bar{\rho}_1 = \bar{\rho}_2$ when the voltage is swept symmetrically, as in Eq. (3.13), and the tunneling rates are equal. As the time populations evolve, the currents at the contact evolve, as is shown in Fig. 4.1(d). During the evolution we can have $I_L \neq I_R$. The currents reach the same stationary value at same time that populations reach an stationary value, verifying the condition $\bar{I}_L = \bar{I}_R$ because of the conservation of electron number.

For the nanojunction in Fig. 4.1(a), the computed current-voltage curve is shown in Fig. 4.2(a). The stationary currents satisfy $\bar{I}_L(V) = \bar{I}_R(V)$, because of the conservation of electron number, while the expression for the stationary currents at bias voltage V , computed using the stationary population in Eq. (4.1) and the definition in Eq. (3.11),

$$\bar{I}_L(V) = \bar{I}_R(V) = e \frac{\gamma_L \gamma_R}{\gamma_L + \gamma_R} \left(f_L^{(2,1)}(V) - f_R^{(2,1)}(V) \right), \quad (4.2)$$

explaining the symmetric behaviour $\bar{I}_{L(R)}(V) = -\bar{I}_{L(R)}(-V)$, when the chemical potentials are swept symmetrically. As is shown in the current-voltage curve, and according to the stationary current in Eq. (4.2), the current is zero at zero bias voltage, and different from zero for a non-zero bias. The stationary current increases (decreases) while the voltage increase (decreases), up to a saturation current at high bias voltage,³ where the fermion densities, $f_L^{(2,1)}(V)$ and $f_R^{(2,1)}(V)$ become constant, verifying that the expression in Eq. (4.2) reduces to the one in [Gurvitz and Prager, 1996, Li et al., 2005]. The sign of the current-voltage curve, means that the electrons are transported through the conducting array from the highest to the lowest chemical potential, having a non-ohmic behaviour.

We expect a peak of conductance at a voltage where the chemical potentials, $\mu_{L(R)}$, are resonant with the transition frequency, $\omega_{n,m}$, because of the energy dependence of the fermionic

³Defined as the bias voltage range where the current reaches a saturation value.

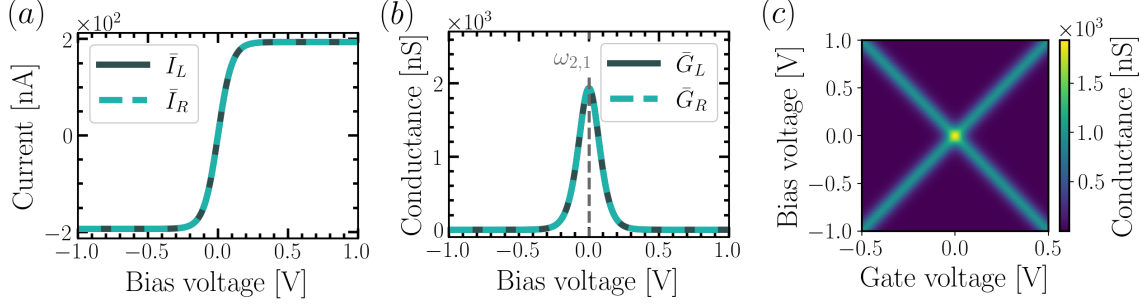


Figure 4.2: For conducting array of $N = 1$ sites with a local ground energy level ε_g , connected to the leads; (a) current-voltage curve; (b) conductance-voltage curve, where vertical dotted lines represent where is satisfied the resonant condition with an transition frequency $\omega_{n,m}$; (c) conductance-voltage as a function of gate voltage. Parameters in Table 4.1.

densities, $f_{L(R)}^{(n,m)}$. The conductance-voltage curve shown in Fig. 4.2(b) shows that the nanojunction in Fig. 4.1(a) has a conductance peak at zero-bias voltage configuration, because it corresponds where both chemical potentials are resonant with the transition frequency $\omega_{2,1} = \omega_g$, represented as a dotted vertical line. When the gate voltage is finite, the changes of the Fermi energy ε_F tend to split and the height of the conductance peaks decreases, as is shown in Fig. 4.2(c), because of the chemical potentials become resonant with the transition frequency $\omega_{2,1}$ one at time for a non-zero bias voltage configurations.

Spin dependent tunneling

The model can take in to account the electronic spin through the index $\sigma = \{\downarrow, \uparrow\}$ for up and down spin, respectively. Consider a conducting array of $N = 1$ site with a degenerate local spin level ε_g , as was illustrated in Fig. 4.1(a), the nanojunction is described by the Hamiltonian,

$$\hat{\mathcal{H}} = \underbrace{\sum_{\sigma} \varepsilon_g \hat{c}_{1,g,\sigma}^\dagger \hat{c}_{1,g,\sigma} + \frac{U}{2} \sum_{\sigma \neq \sigma'} \hat{c}_{1,g,\sigma}^\dagger \hat{c}_{1,g,\sigma'} \hat{c}_{1,g,\sigma'}^\dagger \hat{c}_{1,g,\sigma} + \sum_{l,k,\sigma} \omega_k \hat{c}_{k,l,\sigma}^\dagger \hat{c}_{k,l,\sigma}}_{\hat{\mathcal{H}}_C} + \underbrace{\sum_{l,k,\sigma} u_i^{(l)} \left(V_k^{(l)} \hat{c}_{1,g,\sigma}^\dagger \hat{c}_{l,k,\sigma} + V_k^{(l)*} \hat{c}_{l,k,\sigma}^\dagger \hat{c}_{1,g,\sigma} \right)}_{\hat{\mathcal{H}}_I}, \quad (4.3)$$

Table 4.2: Conducting array eigenstates $\{|e_n\rangle\}$, representation in the Fock space and spectrum $\{\omega_n\}$, for conducting array of $N = 1$ site with a degenerated local ground energy level ε_g and Coulomb repulsion U .

Eigenstates	Fock space	Spectrum
$ e_1\rangle$	$ 0\uparrow, 0\downarrow\rangle$	0
$ e_2\rangle$	$ 0\uparrow, 1\downarrow\rangle$	ε_g
$ e_3\rangle$	$ 1\uparrow, 0\downarrow\rangle$	ε_g
$ e_4\rangle$	$ 1\uparrow, 1\downarrow\rangle$	$2\varepsilon_g + U$

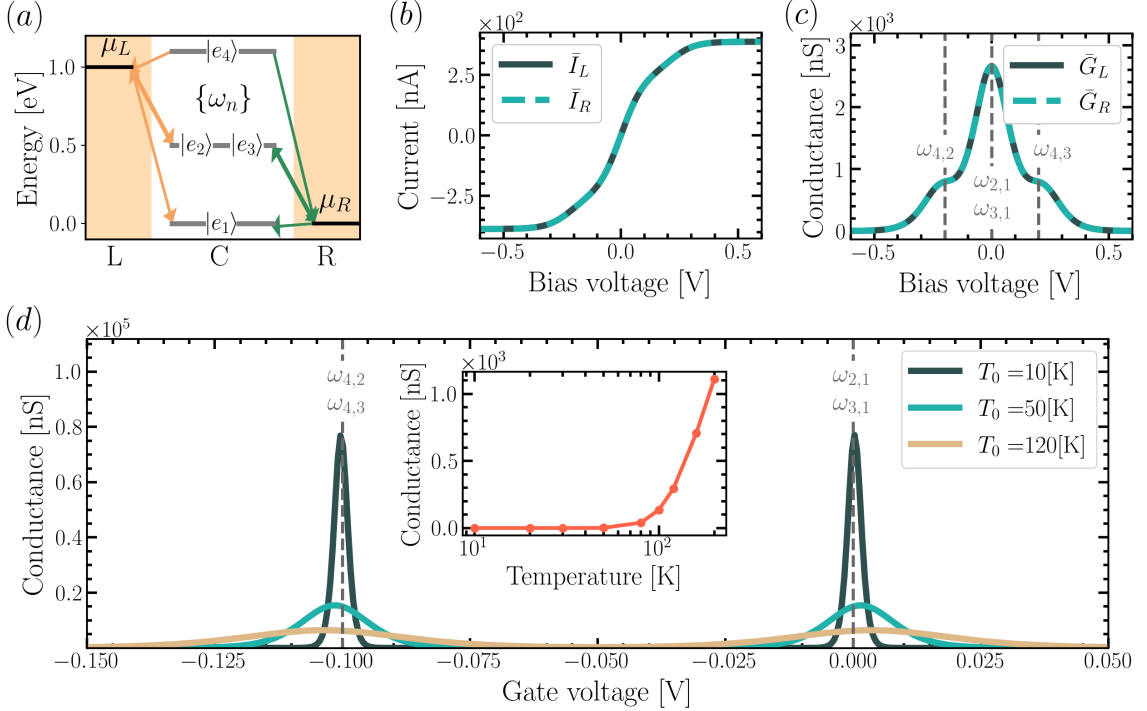


Figure 4.3: For conducting array of $N = 1$ site with degenerate local ground spin level ε_g , connected to the leads; (a) nanojunction energy levels for left lead (L), conducting array (C) and right lead (R), where arrows represent electron transfer induced by left lead (orange), right lead (green), radiation (blue) and phonon (black) at bias voltage of 1[V]; (b) current-voltage curve; (b) conductance-voltage curve, where vertical dotted lines represent where is satisfied the resonant condition with an transition frequency $\omega_{n,m}$; (d) conductance at zero bias voltage as a function of gate voltage for different environment temperatures, where vertical dotted lines represent where is satisfied the resonant condition with an transition frequency $\omega_{n,m}$ (inset: Conductance as a function of temperature on magnetic region). Parameters in Table 4.1.

where $\hat{c}_{1,g,\sigma}$ ($\hat{c}_{1,g,\sigma}^\dagger$) annihilates (creates) an electron in the ground level with spin σ at the conducting array site 1 and $\hat{c}_{k,l,\sigma}$ ($\hat{c}_{k,l,\sigma}^\dagger$) annihilates (creates) an electron in the mode k from lead l with spin σ . We consider the energy of electron in the leads, ω_k , and the coupling, $V_k^{(l)}$, are spin independent.

The nanojunction energy levels in Fig. 4.3(a) shows that the conducting array allows electron tunneling through the leads. When ground local energy levels are fully occupied by the electrons with opposite spins, the Coulomb interaction between them produces a shift in energy U , as is shown for the eigenstate $|e_4\rangle$ in the Table 4.2.

The current-voltage and conductance-voltage curves are shown in Fig. 4.3(b) and (c), respectively. Compared with the case without spin (see Fig. 4.2), both currents are zero at zero-bias voltage and increases (decreases)as the bias voltage increases (decreases), but following a different shape and reaching different saturation currents. In the case with spins the saturation current is almost double the saturation current that the case without spin. The differences are produced because of the possibility of having two electrons in the local energy level ε_g .

When a gate voltage at zero-bias voltage is applied, the resonant condition of tunneling with the leads is affected. Despite the current at zero-bias voltage is zero no matter the gate voltage, the conductance is not necessarily zero, as is shown in Fig. 4.3(d), where a conductance peak at resonant condition is produced, represented by vertical dotted lines. The conductance peaks represent that the conducting array is charging. The separation of conductance peaks in a gate voltage is U , meaning that the Coulomb interaction implies an extra energy for charging the conducting array, which is a Coulomb blockade process.

The thermal dependence of conductance peaks comes from the fermion densities, $f_{L(R)}^{(n,m)}$, which explain why it tends to widen and decreases as the temperature increases. At the middle of the region between the two conductance peaks, known as the magnetic region⁴, the conductance decreases monotonically as the temperature decrease, as is shown in the inset figure.

4.1.2 Spontaneous emission

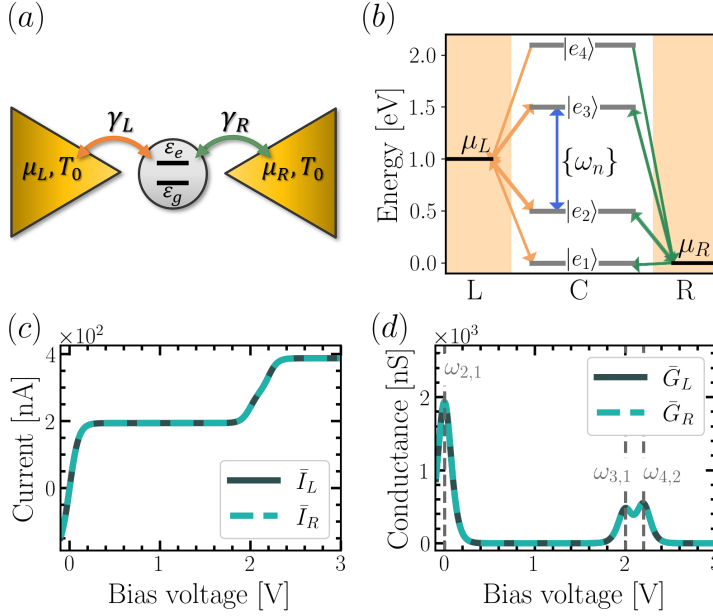


Figure 4.4: For conducting array of $N = 1$ site with local ground and excited energy level ε_g and ε_e , respectively, and coulomb repulsion U , connected to the leads; (a) nanojunction; (b) nanojunction energy levels for left lead (L), conducting array (C) and right lead (R) at bias voltage of 1[V], where arrows represent electron transfer induced by left lead (orange), right lead (green) and radiation (blue); (c) current-voltage curve; (d) conductance-voltage curve, where vertical dotted lines represent where is satisfied the resonant condition with an transition frequency $\omega_{n,m}$. Parameters in Table 4.1.

Consider a conducting array of $N = 1$ sites with local ground and excited energy level ε_g and ε_e , respectively, and Coulomb repulsion energy U , connected to the leads, as illustrated in Fig. 4.4(a). The nanojunction energy levels, shown in Fig. 4.4(b), shows that the system undergoes electron tunneling with the leads and spontaneous emission, being the simplest conducting array that allows this microscopic process. Spontaneous emission induces population transfer between the eigenstate $|e_3\rangle$ to $|e_2\rangle$ (see Table 4.3). The Coulomb interaction appears in the eigenstate $|e_4\rangle$, producing an energy shift U .

The current-voltage curve and conductance-voltage curve are shown in Fig. 4.4(c) and (d), respectively. The stationary current increases as the chemical potential is resonant with the transition energies, which explain the conductance peaks. For the bias voltage region down the resonance $\omega_{3,1}$, the electron transport is equal to the case of conducting array with only local ground energy

⁴The region the configuration of total spin $S = 1/2$ and $S = 0$ [Inoshita, 1998].

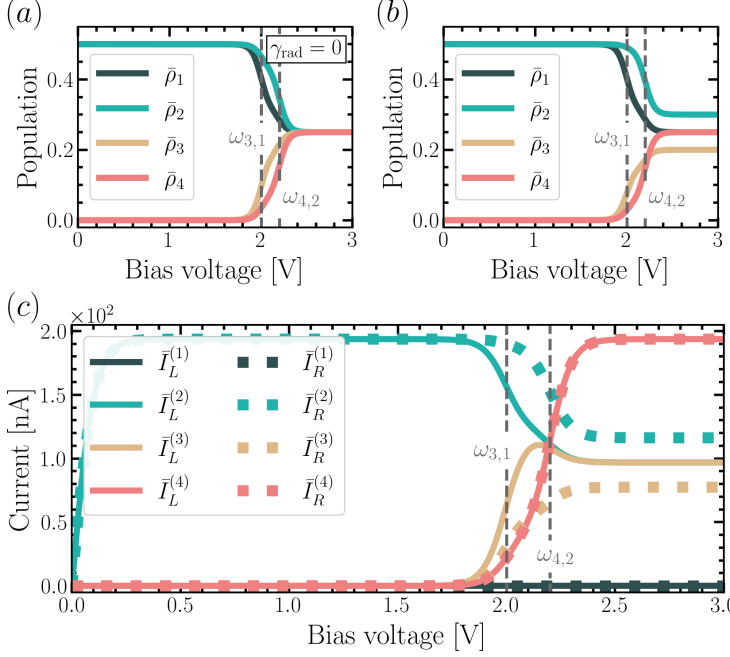


Figure 4.5: For conducting array of $N = 1$ sites with local ground and excited energy level ε_g and ε_e , respectively, and Coulomb repulsion energy U , connected to the leads; stationary populations as a function of voltage when (a) the light-matter interaction is off and (b) the light-matter interaction is on, where vertical dotted lines represent where is satisfied the resonant condition with an transition frequency $\omega_{n,m}$; (c) stationary state dependent currents as a function of voltage, where vertical dotted lines represent where is satisfied the resonant condition with an transition frequency $\omega_{n,m}$. Parameters in Table 4.1.

(see Fig. 4.2), because of the dynamics in this region is produced only by the eigenstates $|e_1\rangle$ and $|e_2\rangle$ only. When the voltage increases, two more conductance peaks are produced by the resonance with the transition frequencies $\omega_{3,1}$ and $\omega_{4,2}$, which increase the current, reaching the saturation value after the third conductance peak.

Table 4.3: Conducting array eigenstates $\{|e_n\rangle\}$, representation in the Fock space and spectrum $\{\omega_n\}$, for conducting array of $N = 1$ site with local ground and excited energy level ε_g and ε_e , respectively, and Coulomb repulsion U .

Eigenstates	Fock space	Spectrum
$ e_1\rangle$	$ 0_g, 0_e\rangle$	0
$ e_2\rangle$	$ 1_g, 0_e\rangle$	ε_g
$ e_3\rangle$	$ 0_g, 1_e\rangle$	ε_e
$ e_4\rangle$	$ 1_g, 1_e\rangle$	$\varepsilon_g + \varepsilon_e + U$

Light-matter interaction in principle incorporates the processes of electron excitation, at rate $\tilde{\kappa}_{\text{rad}}^{(3,2)}$, and spontaneous emission, at rate $\tilde{\kappa}_{\text{rad}}^{(3,2)}$, but, because $\tilde{\kappa}_{\text{rad}}^{(3,2)} \gg \kappa_{\text{rad}}^{(3,2)}$, the net effect of light-matter interaction in the nanojunction dynamics is spontaneous emission. This effect is appreciable in the voltage region where electrons from the leads are tunnelled to the excited levels, which happens after the conductance peaks $\omega_{3,1}$. When light-matter interaction is off (setting $\gamma_{\text{rad}} = 0$), the stationary populations $\bar{\rho}_3$ and $\bar{\rho}_4$ in the bias voltage range after the conductance peak at $\omega_{3,1}$ increase while $\bar{\rho}_1$ and $\bar{\rho}_2$ decrease, up to a value of $\bar{\rho}_1 = \bar{\rho}_2 = \bar{\rho}_3 = \bar{\rho}_4 = 0.25$ at saturation, as shown in Fig. 4.5(a). When light-matter interaction is on, shown in Fig. 4.5(b), in the same bias voltage range the behaviour of stationary populations is similar, but the value of the populations at the saturation configuration is such that $\bar{\rho}_3 < \bar{\rho}_2$, because of the spontaneous emission tends to transfer population from $\bar{\rho}_3$ to $\bar{\rho}_2$.

Although the current-voltage curve satisfies $\bar{I}_L = \bar{I}_R$ along the bias voltage, as was shown in Fig. 4.4(c), it does not happen with the stationary state dependent currents, as is shown in Fig. 4.5(c). The state dependent current in the voltage range after the conductance peak at $\omega_{3,1}$ satisfies $\bar{I}_L^{(2)} < \bar{I}_R^{(2)}$ and $\bar{I}_L^{(3)} > \bar{I}_R^{(3)}$, because spontaneous emission produces the eigenstate $|e_2\rangle$ transfer to the right part of the population which comes from eigenstate $|e_3\rangle$, despite both eigenstates receive the same current from the left lead ($\bar{I}_L^{(2)} = \bar{I}_L^{(3)}$). Therefore, any process different to the leads tunneling which induces transfer of population to a conducting array eigenstate $|e_n\rangle$ will produce that its stationary state dependent current satisfies $\bar{I}_L^{(n)} \neq \bar{I}_R^{(n)}$. This explains why the eigenstates not effected by spontaneous emission satisfy $\bar{I}_L^{(1)} = \bar{I}_R^{(1)}$ and $\bar{I}_L^{(4)} = \bar{I}_R^{(4)}$.

4.1.3 Phonon relaxation

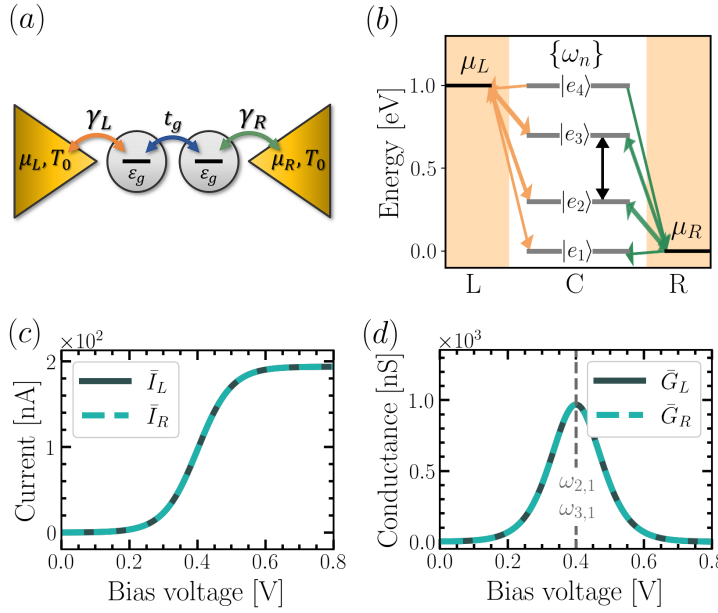


Figure 4.6: For conducting array of $N = 2$ sites with a local ground energy level ε_g , and hopping constant t_g , connected to the leads; (a) nanojunction; (b) nanojunction energy levels for left lead (L), conducting array (C) and right lead (R) at bias voltage of 1[V], where arrows represent electron transfer induced by left lead (orange), right lead (green) and phonon (black); (c) current-voltage curve; (d) conductance-voltage curve, where vertical dotted lines represent where is satisfied the resonant condition with transition frequency $\omega_{n,m}$. Parameters in Table 4.1.

Consider a conducting array of $N = 2$ sites with local ground energy levels ε_g and hopping constant $t_g = t$, connected to the leads, as is illustrated in Fig. 4.6(a). The nanojunction energy levels, shown in Fig. 4.6(b), shows that the tight-binding interaction produces an energy splitting $-t$ and t of the delocalized eigenstates $|e_2\rangle$ and $|e_3\rangle$ (see Table 4.4), respectively. The electron-phonon coupling is included in the dynamics as a phonon relaxation process between the delocalized eigenstates, which produce population transfer between the delocalized eigenstates, being the simplest conducting array which contains the last microscopic process.

Table 4.4: Conducting array eigenstates $\{|e_n\rangle\}$, representation in the Fock space and spectrum $\{\omega_n\}$, for conducting array of $N = 2$ sites with a local ground energy level ε_g , and hopping constant t .

Eigenstates	Fermion Fock space	Spectrum
$ e_1\rangle$	$ 0_g; 0_g\rangle$	0
$ e_2\rangle$	$2^{-1/2} (0_g; 1_g\rangle - 1_g; 0_g\rangle)$	$\varepsilon_g - t$
$ e_3\rangle$	$2^{-1/2} (0_g; 1_g\rangle + 1_g; 0_g\rangle)$	$\varepsilon_g + t$
$ e_4\rangle$	$ 1_g; 1_g\rangle$	$2\varepsilon_g$

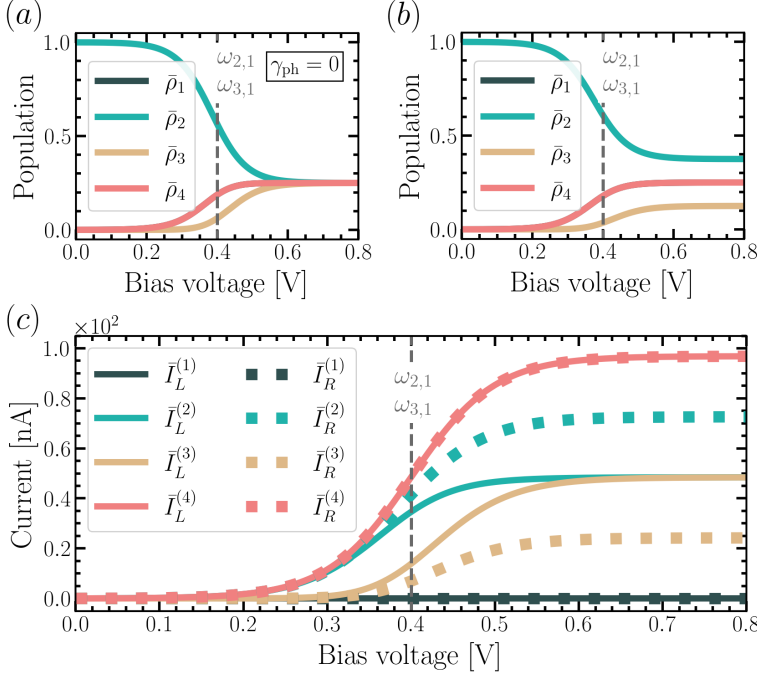


Figure 4.7: For conducting array of $N = 2$ sites with a local ground energy level ε_g , and hopping constant t_g , connected to the leads; stationary populations as a function of voltage when (a) the electron-phonon interaction is off and (b) the electron-phonon interaction is on; (c) stationary state dependent currents as a function of voltage. Parameters in Table 4.1.

The current-voltage and conductance-voltage curve are shown in Fig. 4.6(c) and (d), respectively. The nanojunction begin to performs current when the chemical potentials are resonant with the transition frequencies $\omega_{2,1}$ and $\omega_{3,1}$, related with the conductance peak. Is expected conductance peaks when electrons are tunneled to the delocalized eigenstates, because this states are the only which can connect electrons at the left and right lead. Therefore is explained why there is not current at zero-bias voltage, unlike with the nanojunctions analyzed in Sec. 4.1.1 and Sec. 4.1.2.

In Fig. 4.7(a) and (b) is shown the stationary populations as a function of voltage when the electron-phonon coupling is off ($\gamma_{\text{ph}} = 0$) and on, respectively. In the voltage region down the conductance peak, the stationary population accumulates in the eigenstate $|e_1\rangle$, because it receives preferentially electrons from the left lead, but can not transfer to the right lead because is energetically unfavourable. For the voltage region above the conductance peak, when the electron-phonon interaction is off, all the stationary populations reach the same value at the saturation configuration. However, when electron-phonon interaction is on, the stationary populations at the saturation configuration satisfy $\bar{\rho}_2 > \bar{\rho}_3$. The last difference of population is induced by the phonon relaxation because $\tilde{\kappa}_{\text{ph}}^{(3,2)} \gg \kappa_{\text{ph}}^{(3,2)}$ and the net effect of electron-phonon coupling is transfer population from $|e_3\rangle$ to $|e_2\rangle$, as was discussed for spontaneous emission in Sec 4.1.2.

The state dependent currents as a function of voltage, shown in Fig. 4.7(c), show that for the voltage region above the conductance peak the state dependent currents satisfy $\bar{I}_L^{(2)} \leq \bar{I}_R^{(2)}$ and $\bar{I}_L^{(3)} \geq \bar{I}_R^{(3)}$, while the relations $\bar{I}_L^{(1)} = \bar{I}_R^{(1)}$ and $\bar{I}_L^{(4)} = \bar{I}_R^{(4)}$ are satisfied during all the voltage range. The different between the left and right state dependent current of eigenstates $|e_2\rangle$ and $|e_3\rangle$ is produced because of the eigenstate $|e_2\rangle$ transfers to the right lead also part of the population which comes from eigenstate $|e_3\rangle$, because of the phonon relaxation.

4.2 Geometry array dependence

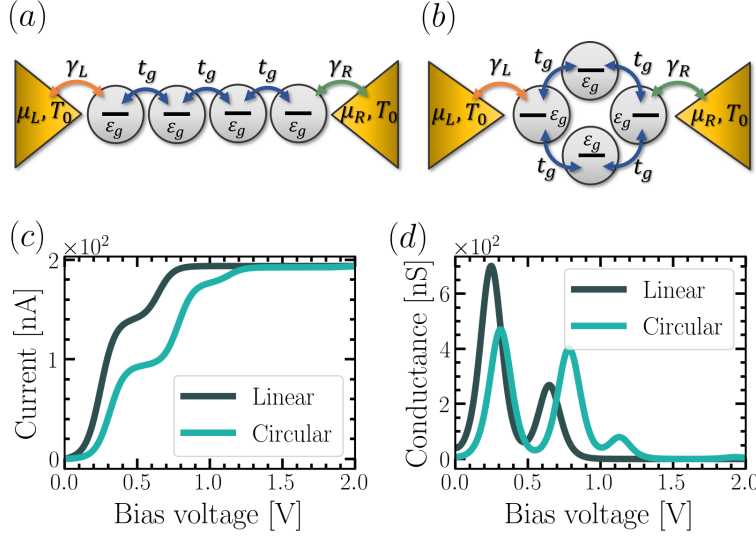


Figure 4.8: For a conducting array of $N = 4$ sites with local ground energy level ε_g , and hopping rates t_g ; nanojunction for (a) linear conducting array and (b) circular conducting array; (c) current-voltage curves for linear and circular conducting array; (d) conductance-voltage curves for linear and circular conducting array. Parameters in Table 4.1.

Consider a conducting array of $N = 4$ sites with local ground energy level ε_g and hopping rate $t_g = t$ in linear and circular geometry, as is illustrated in Fig. 4.8(a) and (b), respectively. Both nanojunctions undergo electron tunneling with the leads and phonon relaxation. The differences between them is the hopping interaction, because in the circular geometry is added hopping interaction between the sites $i = 4$ and $i = 1$, and the sites which connected to the leads, because of the right lead coupling with the conducting site $i = 4$ for linear array and with the conducting site $i = 3$ for circular array.

The current-voltage curves for both geometries are shown in Fig. 4.8(c). The difference of current-voltage curves are explained by the different hopping interactions, which change the conducting array eigenstates and spectrum, and the different sites which interact with the leads, which produce populations transfer between different sets of eigenstates at different rates. These reasons also explain why the conductance peaks are localized at different bias-voltages and have different sizes, as is shown in Fig. 4.8(d). Although, the both current looks like a displacement of one respect to the other, reaching a common value of its saturation currents. Comparing the saturation current values of conducting arrays based on ground local levels (see Fig. 4.2(a) and 4.6(c)), all of them have similar value. Therefore, the value of saturation current is limited principally by considering one local energy level, not by the conducting array geometry.

The stationary state dependent current for linear and circular conducting array at the saturation configuration are shown in Fig. 4.9(a) and (b), respectively. For both geometries, the states dependent contribution looks similar as a function of n , which only enumerates the eigenstates from lowest to highest energy. Almost all of the state dependent current are different at the right and left for the set of eigenstates, because of the presence of phonon relaxation, as we discussed in Sec. 4.1.3. When the electron-phonon interaction is off ($\gamma_{\text{ph}} = 0$) all the state dependent current satisfies $\bar{I}_L^{(n)} = \bar{I}_R^{(n)}$ for all the set of eigenstates, as is shown in Fig. 4.9(c) and (d) for linear and circular conducting array, respectively.

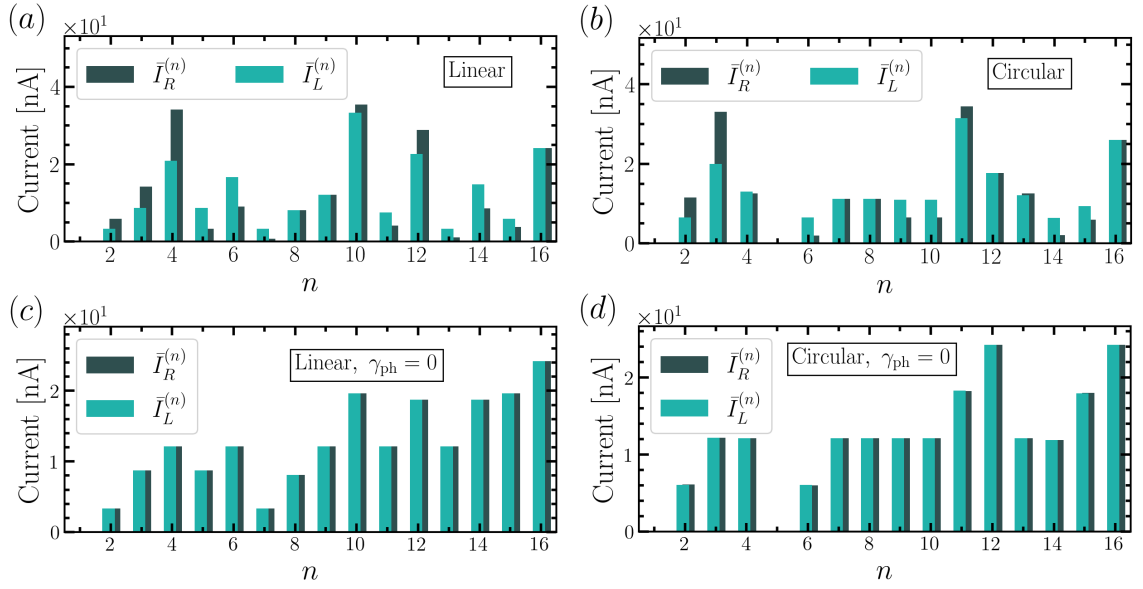


Figure 4.9: For a conducting array of $N = 4$ sites with local ground energy levels ε_g , and hopping rates t_g ; state dependent current at 2[V] bias voltage for (a) linear conducting array and (b) circular conducting array; and when the electron-phonon interaction is off ($\gamma_{ph} = 0$) for (c) linear conducting array and (d) circular conducting array. Parameters in Table 4.1.

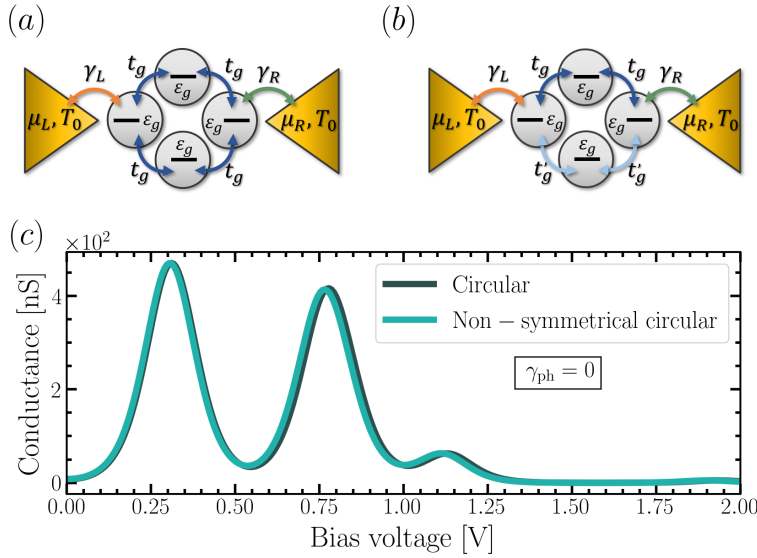


Figure 4.10: For a circular conducting array of $N = 4$ sites with local ground energy levels ε_g ; (a) nanojunction for symmetric hopping rates t_g ; (b) nanojunction for non-symmetrical hopping rates of t_g for upper path and t'_g for lower path; (c) current-voltage curves for circular symmetric and non-symmetrical conducting array. Parameters in Table 4.1.

In multiple-path systems, the wave function, as a complex number, can interfere during the transport, increasing or decreasing the tunneling for constructive and destructive interference, respectively [Taylor et al., 2002]. The process of quantum interference must be maximum when the electron path are indistinguishable, as the upper and lower path in the case of circular array shown in Fig. 4.10(a). Therefore, when the path are slightly distinguishable, as the non-symmetrical circular conducting array shown in Fig. 4.10(b) where the hopping rate for the upper and lower paths are $t_g = t$ and $t_g' = 0.97t$, respectively, the quantum interference effect must be minimized. In Fig. 4.10(c) are shown the conductance-voltage curves for circular symmetric and non-symmetrical conducting array, where we fix $\gamma_{\text{ph}} = 0$ for observing only the tunneling dynamics. The slightly different of their conductance-voltage curves comes from the changes of eigenstates and energies, but is not observed any suppression of currents because of the quantum interference, as is expected in this kind of systems [Solomon et al., 2009].

4.3 Incoherent pumping

In the presence of a light source, molecular junctions has demonstrated the phenomena of light-induced current [Lara-Avila et al., 2011, Battacharyya et al., 2011], measured as an enhancement of current due the creation of excited-state molecule, and current-induced light [Qiu et al., 2003, Wu et al., 2008], measured as luminescence because of the tunneled excited electrons. Both effects has been also studied theoretically in [Galperin and Nitzan, 2005, Galperin and Nitzan, 2006].

In a two-level system, an applied source of incoherent light excites electrons from the local ground to the excited level incoherently. If this source is applied to the conducting array, in the perturbative regime the effect on the nanojunction dynamics is taken in to account adding the dissipative term

$$\sum_i W_{\text{Ext}} \left(\hat{c}_{i,e}^\dagger \hat{c}_{i,g} \hat{\rho}_C(t) \left(\hat{c}_{i,e}^\dagger \hat{c}_{i,g} \right)^\dagger - \frac{1}{2} \left\{ \left(\hat{c}_{i,e}^\dagger \hat{c}_{i,g} \right)^\dagger \hat{c}_{i,e}^\dagger \hat{c}_{i,g}, \hat{\rho}_C(t) \right\} \right), \quad (4.4)$$

in the Lindblad quantum master equation in Eq. (3.4). We consider the pumping rate, W_{Ext} , as a constant because we assume a constant spectral density in the range of transition frequencies. In the secular approximation, the dissipator in Eq. (4.4) in the energy basis is reduced to

$$\sum_{n,m} \kappa_{\text{Ext}}^{(n,m)} \mathcal{L}_{n,m} [\hat{\rho}_C(t)], \quad \kappa_{\text{Ext}}^{(n,m)} = W_{\text{Ext}} | \langle e_n | \sum_i \hat{c}_{i,e}^\dagger \hat{c}_{i,g} | e_m \rangle |^2, \quad (4.5)$$

which means that the incoherent pumping induces electron transitions between the conducting array eigenstates $|e_m\rangle \rightarrow |e_n\rangle$ with effective transfer rate $\kappa_{\text{Ext}}^{(n,m)}$. The effective transfer rates of pumping in Eq. (4.5) follow the same selection rules of eigenstates than excitation by photons, $\kappa_{\text{rad}}^{(n,m)}$ (see details in Table B.2).

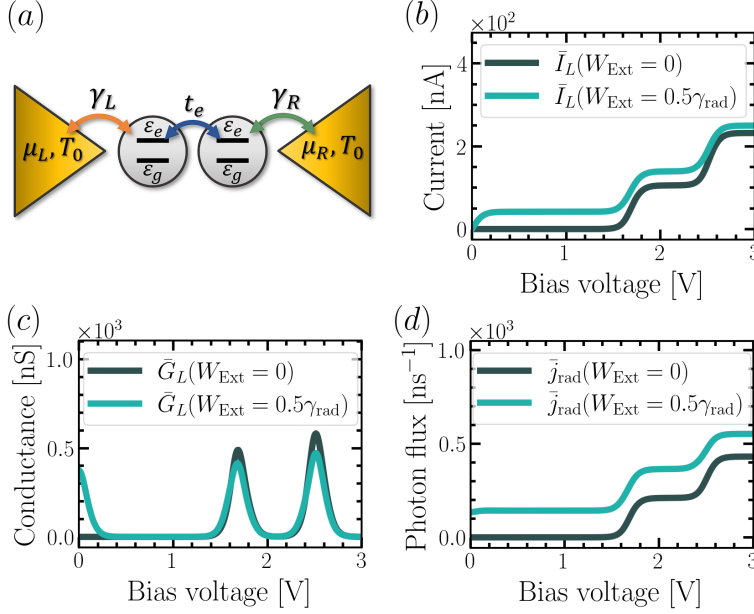


Figure 4.11: For conducting array of $N = 2$ sites with local ground and excited energy level ε_g and ε_e , respectively, Coulomb repulsion energy U and hopping rate t_e through the local excited energy level, connected to the leads; (a) nanojunction; (b) current-voltage curve as a function of incoherent pumping rate; (c) conductance-voltage curve as a function of incoherent pumping rate; (d) stationary photon flux as a function of bias voltage and pumping rate. Parameters in Table 4.1.

Consider a conducting array with $N = 2$ sites⁵ with local energy levels ε_g and ε_e , Coulomb repulsion energy U and hopping rate $t_e = t$ only between the excited levels, connected to the leads, as is illustrated in Fig. 4.11(a). The nanojunction undergoes electron tunneling with the leads, spontaneous emission and phonon relaxation.

The effect of incoherent pumping in the current-voltage curve is shown in the Fig. 4.11(b), where we consider W^{Ext} up to $0.5\gamma_{\text{rad}}$ for being considered as a perturbation and being valid the two-level approximation. It is shown that incoherent pumping produces an offset of current respect to the case without pumping, as a light-induced current process, but conserving similar shape. The incoherent pumping increases the stationary current intermediately when the bias voltage appears, because it transfers electrons from the localized ground eigenstates to the delocalized excited eigenstates, from where the electrons could tunnel preferentially to the lower chemical potentials, which explains the conductance peak at zero bias voltage shown in Fig. 4.11(c). After the first conductance peaks, both current-voltage curves have similar bias voltage dependence, because this region the voltage range the current comes from the electrons tunneled from the leads to the excited eigenstates. With or without incoherent pumping, both currents reach similar saturation value. The saturation currents are less than obtained from other nanojunction based on conducting array with two local energy levels (see Fig. 4.4(c)).

Let \hat{N}_{rad} be number operator of photons in the radiation, the stationary photon flux emitted by the conducting array is defined as (see derivation in Appendix C)

$$\bar{j}_{\text{rad}} = \frac{d}{dt} \langle \hat{N}_{\text{rad}} \rangle = - \sum_{n,m} \left(\kappa_{\text{rad}}^{(n,m)} \bar{\rho}_m - \tilde{\kappa}_{\text{rad}}^{(n,m)} \bar{\rho}_n \right), \quad (4.6)$$

which quantifies the number of photons per unit of time added to the radiation field by the non-equilibrium conducting array dynamics. As is shown in Fig. 4.11(d), the incoherent pumping

⁵It was verified that incoherent pumping in the case of conducting array with $N = 1$ sites in Fig. 4.4(a) does not affect the electron transport, because it only tends to apposite the effect of spontaneous emission.

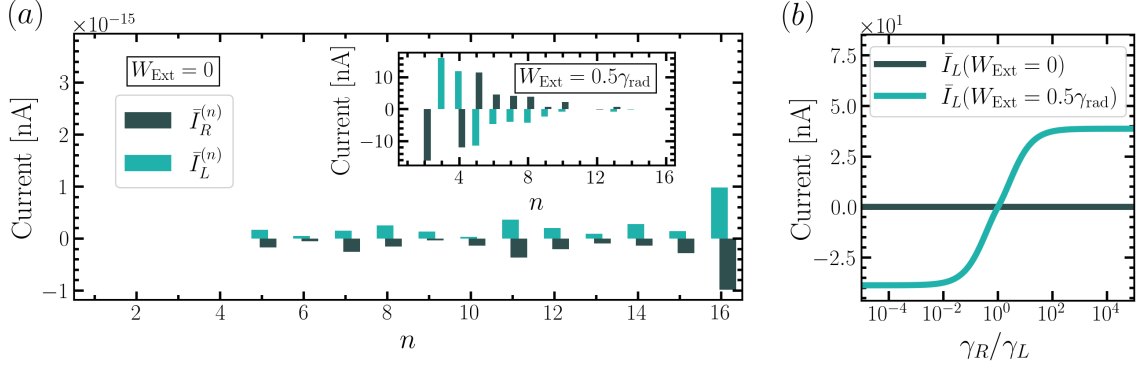


Figure 4.12: For conducting array of $N = 2$ sites with local ground and excited energy level ε_g and ε_e , respectively, Coulomb repulsion energy U and hopping rate t_e through the local excited level, connected to the leads; (a) state dependent currents at 0[V] bias voltage without incoherent pumping ($W_{\text{Ext}} = 0$); (b) stationary current at 0[V] bias voltage as a function of incoherent pumping and tunneling rates. Parameters in Table 4.1.

increases the photon flux respect to the case without it, because of the electrons excited by the incoherent pumping can decay by spontaneous emission, emitting photons in the process. Both curves have the similar bias voltage dependence, because of the increasing of photon flux is produced by electrons which previously have been tunneled from the leads to the excited delocalized eigenstates, as current-induced light process.

When we focus on the zero-bias voltage configuration, despite the stationary currents in the nanojunction are zero no matter the incoherent pumping rate (see Fig. 4.11(b)), some stationary state dependent currents, shown in Fig. 4.12(a), have positive and negative values, which satisfy $\bar{I}_L^{(n)} \neq \bar{I}_R^{(n)}$. When the incoherent pumping is off, the stationary state dependent currents are low ($\approx 10^{-15}[\text{nA}]$) respect to the saturation current reached by the system ($\approx 10^2[\text{nA}]$). However, it is not so the case when the incoherent pumping is applied, where there are significant state dependent currents ($\approx 10^1[\text{nA}]$). Those significant stationary state dependent current are produced because of the electrons, which originally are in the localized ground eigenstates, are excited to the delocalized excited eigenstates, which produces that the empty localized ground eigenstates can receives electrons from the leads, while the electrons in the delocalized excited eigenstates can tunnels to the leads. Even so, the stationary current, as the sum of all the state dependent currents in their respective leads, is zero in the both contacts when the pumping is applied because of the tunneling process does not prefer any specific direction when the tunneling rates are equal. Nevertheless, when $\gamma_R \neq \gamma_L$ ⁶, an stationary photocurrent is induced to the right if $\gamma_R > \gamma_L$ or to the left if $\gamma_R < \gamma_L$ at zero bias voltages, as is shown in Fig. 4.12(b). The stationary photocurrent at zero bias voltage has a maximum value of approximately 15% of the saturation current of the nanojunction. Photocurrents at zero bias voltage when the tunneling rates are different have been predicted before in [Galperin and Nitzan, 2005, Galperin and Nitzan, 2006] for similar systems.

⁶The tunneling rates are modifying increasing their values respect to the given in Table 4.1.

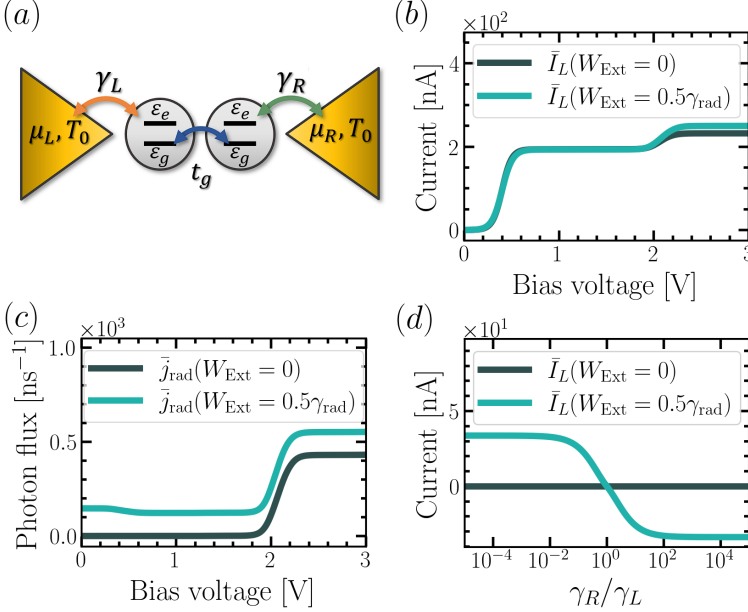


Figure 4.13: For conducting array of $N = 2$ sites with local ground and excited energy level ε_g and ε_e , respectively, Coulomb repulsion energy U and hopping rate t_g through the local ground level, connected to the leads; (a) nanojunction; (b) current-voltage curve as a function of incoherent pumping rate; (c) stationary photon flux as a function of bias voltage and pumping rate; (d) stationary current at 0[V] bias voltage as a function of incoherent pumping rate and tunneling rates. Parameters in Table 4.1.

When the conducting array in Fig. 4.11(a) has a hopping constant $t_g = t$ only between the ground levels, the nanojunction is illustrated in the Fig. 4.13(a). The nanojunction also undergoes electron tunneling with the leads, spontaneous emission and phonon relaxation, but with different rates and set of eigenstates.

Because of the nanojunction is delocalized in the ground eigenstates, is expected the stationary current is not considerably enhanced by the incoherent pumping, as is shown in Fig. 4.13(b), because of the spontaneous tends to naturally delocalize the electrons.

Because of the incoherent pumping is constantly exciting electrons, is expected an increase of the stationary photon flux respect to the case without it, as is shown in Fig. 4.13(c). The bias voltage dependence of photon flux for both cases look similar, because is the current-induced light process.

Because of the non-equilibrium dynamics induced by the incoherent pumping at zero bias voltage condition, when the tunneling rates at left and right contacts are different in the nanojunction in Fig 4.13(a), stationary photocurrent is induced to the left if $\gamma_R > \gamma_L$ and to the right when $\gamma_R < \gamma_L$, with a maximum value of approximately 15% of the saturation current. Compared with the case of hopping in the excited levels (see Fig. 4.12(b)), the stationary photocurrent at zero voltage configuration varies between similar values. Nevertheless, the direction of photocurrent is the opposite. This difference of the direction is explained because, while the conducting array delocalized in the excited levels only transfers electrons from the delocalized excited eigenstates preferentially to the lead with higher tunneling rates, producing stationary current to the higher tunneling direction, the conducting array delocalized in the ground levels only receives electrons preferentially from the lead with higher tunneling rate to the delocalized ground eigenstates, producing stationary current to the lower tunneling direction.

Conclusions

In this Thesis, we study electron transport in driven nanojunctions. We use the second quantization formalism to describe a nanojunction composed of an array of conducting sites coupled to electronic leads. Conducting sites can represent individual quantum dots or single conjugated molecules. We study the current-voltage dynamics of the nanojunction using the density matrix formalism discussed, solving for the transient and steady-state response of the conducting system by numerically integrating the corresponding Lindblad quantum master equation using Python code developed for this Thesis. Driven-dissipative electron transport systems are common in natural and artificial scenarios. The dissipative operators and rates were defined in agreement previous work in the literature, resulting in analytical expressions for the electron currents through the system that were in agreement with previous work [Gurvitz and Prager, 1996, Li et al., 2005]. The simplicity of our nanojunction model offers simple and intuitive tools for describing electron transport in nanojunctions. The decoupling of populations and coherences in our Lindblad formalism, ensures that the nanojunction dynamics is reduced only to the evolution of population, which could be useful for analyzing electron transport through complex conducting arrays, because of the dimensionality of the system dynamics then scales only linearly with the system dimension, while others full quantum master equations scale in principle quadratically with the system dimension.

Under the influence of an external voltage, we studied the dependence of the current-voltage curves on the number of array sites, the geometry of the conducting array, the magnitude of the state-dependent electron tunneling rates, the electron-phonon coupling strength, and the spontaneous emission rate. Additionally, we study the influence of an incoherent light source that pumps energy into the conducting array, on the state-dependent electron current and photon flux through the system. Our results show that resonant electron tunneling explains the positions of the conductance peaks, while spontaneous emission and phonon relaxation processes explain the possible difference between left and right stationary currents for individual system eigenstates. We also show that the electron transport depends on the geometry of the conducting array, for fixed number of sites and local energy levels. When the incoherent pumping source is applied on a delocalized electron state within the array, our results agree with the results obtained in [Galperin and Nitzan, 2005, Galperin and Nitzan, 2006], which for a similar system predict light-induced current and current-induced light, and the non-equilibrium dynamics induced with the leads at zero bias voltage can be reflected in stationary photocurrent when the left-right tunneling rates are different. The direction of the induced photocurrent depends on whether the conducting array has delocalized electrons in the ground or the excited orbital manifolds.

Given our simplified Lindblad master equation approach, several interesting phenomena fall outside of the scope of this Thesis, including polaron effects and other Non-Markovian system-environment interactions that may be relevant in experiments. In the near future, our work can be extended to describe charge and excitation transfer in nanojunction that are strongly coupled to quantized electromagnetic fields, under conditions that favor the formation of hybrid polariton states that are part light and part matter. Experimental [Orgiu et al., 2015, Chikkaraddy et al., 2016] and theoretical [Hagenmüller et al., 2017, Hagenmüller et al., 2018, Schäfer et al., 2019] studies have reported enhanced of currents relative to cavity-free scenario by orders of magnitude. These enhanced currents have been associated with vacuum-induced electron-electron correlations over large distances, and the formation of coherent states which extend over hundreds of molecules. Possible applications of these transport enhancements are currently under intense investigation in the emerging field of molecular polaritons [Herrera and Owrutsky, 2020].

Bibliography

- [Andergassen et al., 2010] Andergassen, S., Meden, V., Schoeller, H., Splettstoesser, J., and Wegewijs, M. (2010). Charge transport through single molecules, quantum dots and quantum wires. *Nanotechnology*, 21(27):272001.
- [Aviram and Ratner, 1974] Aviram, A. and Ratner, M. A. (1974). Molecular rectifiers. *Chemical physics letters*, 29(2):277–283.
- [Ballmann et al., 2012] Ballmann, S., Härtle, R., Coto, P. B., Elbing, M., Mayor, M., Bryce, M. R., Thoss, M., and Weber, H. B. (2012). Experimental evidence for quantum interference and vibrationally induced decoherence in single-molecule junctions. *Physical review letters*, 109(5):056801.
- [Battacharyya et al., 2011] Battacharyya, S., Kibel, A., Kodis, G., Liddell, P. A., Gervaldo, M., Gust, D., and Lindsay, S. (2011). Optical modulation of molecular conductance. *Nano letters*, 11(7):2709–2714.
- [Breuer et al., 2002] Breuer, H.-P., Petruccione, F., et al. (2002). *The theory of open quantum systems*. Oxford University Press on Demand.
- [Bruus and Flensberg, 2004] Bruus, H. and Flensberg, K. (2004). *Many-body quantum theory in condensed matter physics: an introduction*. Oxford university press.
- [Burzurí et al., 2014] Burzurí, E., Yamamoto, Y., Warnock, M., Zhong, X., Park, K., Cornia, A., and van der Zant, H. S. (2014). Franck–condon blockade in a single-molecule transistor. *Nano letters*, 14(6):3191–3196.
- [Chikkaraddy et al., 2016] Chikkaraddy, R., De Nijs, B., Benz, F., Barrow, S. J., Scherman, O. A., Rosta, E., Demetriadou, A., Fox, P., Hess, O., and Baumberg, J. J. (2016). Single-molecule strong coupling at room temperature in plasmonic nanocavities. *Nature*, 535(7610):127–130.
- [Esposito and Galperin, 2009] Esposito, M. and Galperin, M. (2009). Transport in molecular states language: Generalized quantum master equation approach. *Physical Review B*, 79(20):205303.
- [Esposito and Galperin, 2010] Esposito, M. and Galperin, M. (2010). Self-consistent quantum master equation approach to molecular transport. *The Journal of Physical Chemistry C*, 114(48):20362–20369.

- [Evers et al., 2020] Evers, F., Korytár, R., Tewari, S., and van Ruitenbeek, J. M. (2020). Advances and challenges in single-molecule electron transport. *Reviews of Modern Physics*, 92(3):035001.
- [Galperin and Nitzan, 2005] Galperin, M. and Nitzan, A. (2005). Current-induced light emission and light-induced current in molecular-tunneling junctions. *Physical review letters*, 95(20):206802.
- [Galperin and Nitzan, 2006] Galperin, M. and Nitzan, A. (2006). Optical properties of current carrying molecular wires. *The Journal of chemical physics*, 124(23):234709.
- [Galperin et al., 2006] Galperin, M., Nitzan, A., and Ratner, M. A. (2006). Resonant inelastic tunneling in molecular junctions. *Physical Review B*, 73(4):045314.
- [Gauger et al., 2008] Gauger, E. M., Nazir, A., Benjamin, S. C., Stace, T. M., and Lovett, B. W. (2008). Robust adiabatic approach to optical spin entangling in coupled quantum dots. *New Journal of Physics*, 10(7):073016.
- [Gehring et al., 2019] Gehring, P., Thijssen, J. M., and van der Zant, H. S. (2019). Single-molecule quantum-transport phenomena in break junctions. *Nature Reviews Physics*, 1(6):381–396.
- [Greiner et al., 2012] Greiner, W., Neise, L., and Stöcker, H. (2012). *Thermodynamics and statistical mechanics*. Springer Science & Business Media.
- [Gurvitz and Prager, 1996] Gurvitz, S. and Prager, Y. S. (1996). Microscopic derivation of rate equations for quantum transport. *Physical Review B*, 53(23):15932.
- [Hagenmüller et al., 2017] Hagenmüller, D., Schachenmayer, J., Schütz, S., Genes, C., and Pupillo, G. (2017). Cavity-enhanced transport of charge. *Physical review letters*, 119(22):223601.
- [Hagenmüller et al., 2018] Hagenmüller, D., Schütz, S., Schachenmayer, J., Genes, C., and Pupillo, G. (2018). Cavity-assisted mesoscopic transport of fermions: Coherent and dissipative dynamics. *Physical Review B*, 97(20):205303.
- [Harbola et al., 2006] Harbola, U., Esposito, M., and Mukamel, S. (2006). Quantum master equation for electron transport through quantum dots and single molecules. *Physical Review B*, 74(23):235309.
- [Herrera and Owrusky, 2020] Herrera, F. and Owrusky, J. (2020). Molecular polaritons for controlling chemistry with quantum optics. *The Journal of chemical physics*, 152(10):100902.
- [Hoang et al., 2015] Hoang, T. B., Akselrod, G. M., Argyropoulos, C., Huang, J., Smith, D. R., and Mikkelsen, M. H. (2015). Ultrafast spontaneous emission source using plasmonic nanoantennas. *Nature communications*, 6(1):1–7.
- [Hubbard, 1963] Hubbard, J. (1963). Electron correlations in narrow energy bands. *Proceedings of the Royal Society of London. Series A. Mathematical and Physical Sciences*, 276(1365):238–257.

- [Hubbard, 1967] Hubbard, J. (1967). Electron correlations in narrow energy bands v. a perturbation expansion about the atomic limit. *Proceedings of the Royal Society of London. Series A. Mathematical and Physical Sciences*, 296(1444):82–99.
- [Inoshita, 1998] Inoshita, T. (1998). Kondo effect in quantum dots. *Science*, 281(5376):526–527.
- [Jeong et al., 2001] Jeong, H., Chang, A. M., and Melloch, M. R. (2001). The kondo effect in an artificial quantum dot molecule. *Science*, 293(5538):2221–2223.
- [Kondo, 1964] Kondo, J. (1964). Resistance minimum in dilute magnetic alloys. *Progress of theoretical physics*, 32(1):37–49.
- [Kouwenhoven, 1995] Kouwenhoven, L. (1995). Coupled quantum dots as artificial molecules. *Science*, 268(5216):1440–1442.
- [Kouwenhoven et al., 1991] Kouwenhoven, L., van der Vaart, N., Johnson, A., Wool, K., and EJ, C. (1991). Harmans, jg williamson, and aam staring. *Z. Phys. B*, 85:367.
- [Kouwenhoven et al., 1997] Kouwenhoven, L. P., Marcus, C. M., McEuen, P. L., Tarucha, S., Westervelt, R. M., and Wingreen, N. S. (1997). Electron transport in quantum dots. In *Mesoscopic electron transport*, pages 105–214. Springer.
- [Lara-Avila et al., 2011] Lara-Avila, S., Danilov, A. V., Kubatkin, S. E., Broman, S. L., Parker, C. R., and Nielsen, M. B. (2011). Light-triggered conductance switching in single-molecule dihydroazulene/vinylheptafulvene junctions. *The Journal of Physical Chemistry C*, 115(37):18372–18377.
- [Leturcq et al., 2009] Leturcq, R., Stampfer, C., Inderbitzin, K., Durrer, L., Hierold, C., Mariani, E., Schultz, M. G., Von Oppen, F., and Ensslin, K. (2009). Franck–condon blockade in suspended carbon nanotube quantum dots. *Nature Physics*, 5(5):327–331.
- [Li et al., 2005] Li, X.-Q., Luo, J., Yang, Y.-G., Cui, P., and Yan, Y. (2005). Quantum master-equation approach to quantum transport through mesoscopic systems. *Physical Review B*, 71(20):205304.
- [Liu and Segal, 2020] Liu, J. and Segal, D. (2020). Generalized input-output method to quantum transport junctions. ii. applications. *Physical Review B*, 101(15):155407.
- [Mahan, 2013] Mahan, G. D. (2013). *Many-particle physics*. Springer Science & Business Media.
- [Nitzan, 2006] Nitzan, A. (2006). *Chemical dynamics in condensed phases: relaxation, transfer and reactions in condensed molecular systems*. Oxford university press.
- [Nitzan and Ratner, 2003] Nitzan, A. and Ratner, M. A. (2003). Electron transport in molecular wire junctions. *Science*, 300(5624):1384–1389.
- [Nolting et al., 2018] Nolting, W. et al. (2018). *Theoretical Physics 8*. Springer.
- [Orgiu et al., 2015] Orgiu, E., George, J., Hutchison, J., Devaux, E., Dayen, J., Doudin, B., Stellacci, F., Genet, C., Schachenmayer, J., Genes, C., et al. (2015). Conductivity in organic semiconductors hybridized with the vacuum field. *Nature Materials*, 14(11):1123–1129.

- [Park et al., 2002] Park, J., Pasupathy, A. N., Goldsmith, J. I., Chang, C., Yaish, Y., Petta, J. R., Rinkoski, M., Sethna, J. P., Abruña, H. D., McEuen, P. L., et al. (2002). Coulomb blockade and the kondo effect in single-atom transistors. *Nature*, 417(6890):722–725.
- [Pedersen and Wacker, 2005] Pedersen, J. N. and Wacker, A. (2005). Tunneling through nanosystems: Combining broadening with many-particle states. *Physical Review B*, 72(19):195330.
- [Perrin et al., 2014] Perrin, M. L., Frisenda, R., Koole, M., Seldenthuis, J. S., Gil, J. A. C., Valkenier, H., Hummelen, J. C., Renaud, N., Grozema, F. C., Thijssen, J. M., et al. (2014). Large negative differential conductance in single-molecule break junctions. *Nature nanotechnology*, 9(10):830.
- [Qiu et al., 2003] Qiu, X., Nazin, G., and Ho, W. (2003). vibrationally resolved fluorescence excited with submolecular precision. *Science*, 299(5606):542–546.
- [Reed et al., 1997] Reed, M. A., Zhou, C., Muller, C., Burgin, T., and Tour, J. (1997). Conductance of a molecular junction. *Science*, 278(5336):252–254.
- [Reimann and Manninen, 2002] Reimann, S. M. and Manninen, M. (2002). Electronic structure of quantum dots. *Reviews of modern physics*, 74(4):1283.
- [Schäfer et al., 2019] Schäfer, C., Ruggenthaler, M., Appel, H., and Rubio, A. (2019). Modification of excitation and charge transfer in cavity quantum-electrodynamical chemistry. *Proceedings of the National Academy of Sciences*, 116(11):4883–4892.
- [Scheer and Cuevas, 2017] Scheer, E. and Cuevas, J. C. (2017). *Molecular electronics: an introduction to theory and experiment*, volume 15. World Scientific.
- [Solomon et al., 2009] Solomon, G. C., Andrews, D. Q., Van Duyne, R. P., and Ratner, M. A. (2009). Electron transport through conjugated molecules: When the π system only tells part of the story. *ChemPhysChem*, 10(1):257–264.
- [Sowa et al., 2017] Sowa, J. K., Mol, J. A., Briggs, G. A. D., and Gauger, E. M. (2017). Vibrational effects in charge transport through a molecular double quantum dot. *Physical Review B*, 95(8):085423.
- [Sowa et al., 2018] Sowa, J. K., Mol, J. A., Briggs, G. A. D., and Gauger, E. M. (2018). Beyond marcus theory and the landauer-büttiker approach in molecular junctions: A unified framework. *The Journal of chemical physics*, 149(15):154112.
- [Tartakovskii, 2012] Tartakovskii, A. (2012). Quantum dots: optics, electron transport and future applications.
- [Tarucha et al., 1996] Tarucha, S., Austing, D., Honda, T., Van der Hage, R., and Kouwenhoven, L. P. (1996). Shell filling and spin effects in a few electron quantum dot. *Physical Review Letters*, 77(17):3613.
- [Taylor et al., 2002] Taylor, J., Brandbyge, M., and Stokbro, K. (2002). Theory of rectification in tour wires: The role of electrode coupling. *Physical review letters*, 89(13):138301.

- [Thoss and Evers, 2018] Thoss, M. and Evers, F. (2018). Perspective: Theory of quantum transport in molecular junctions. *The Journal of chemical physics*, 148(3):030901.
- [Timm, 2008] Timm, C. (2008). Tunneling through molecules and quantum dots: Master-equation approaches. *Physical Review B*, 77(19):195416.
- [Wu et al., 2008] Wu, S., Nazin, G., and Ho, W. (2008). Intramolecular photon emission from a single molecule in a scanning tunneling microscope. *Physical Review B*, 77(20):205430.
- [Xue et al., 1999] Xue, Y., Datta, S., Hong, S., Reifenberger, R., Henderson, J. I., and Kubiak, C. P. (1999). Negative differential resistance in the scanning-tunneling spectroscopy of organic molecules. *Physical Review B*, 59(12):R7852.
- [Yoffe, 2001] Yoffe, A. D. (2001). Semiconductor quantum dots and related systems: electronic, optical, luminescence and related properties of low dimensional systems. *Advances in physics*, 50(1):1–208.

Appendix A

Redfield equation

Writing the nanojunction Hamiltonian in Eq. (2.22) as

$$\hat{\mathcal{H}} = \hat{\mathcal{H}}_0 + \hat{\mathcal{H}}_I, \quad \hat{\mathcal{H}}_0 = \hat{\mathcal{H}}_C + \hat{\mathcal{H}}_E, \quad (\text{A.1})$$

any operator $\hat{\mathcal{A}}$ in the Schrödinger picture could be written in interaction picture $\hat{\mathcal{A}}^*(t)$ respect to $\hat{\mathcal{H}}_I$, and vice versa, following the transformations

$$\hat{\mathcal{A}}^*(t) = \hat{U} \hat{\mathcal{A}} \hat{U}^\dagger, \quad \hat{\mathcal{A}} = \hat{U}^\dagger \hat{\mathcal{A}}^*(t) \hat{U}, \quad (\text{A.2})$$

where the operator $\hat{U} = \exp(i\hat{\mathcal{H}}_0 t)$ is a unitary transformation.

The Liouville equation (see Eq. (2.8)) for the nanojunction density operator in the interaction picture $\hat{\rho}^*$ becomes

$$\frac{d}{dt} \hat{\rho}^*(t) = -i [\hat{\mathcal{H}}_I(t), \hat{\rho}^*(t)], \quad (\text{A.3})$$

where $\hat{\mathcal{H}}_I(t)$ is the Hamiltonian interaction in the interaction picture. Applying direct integration from t_0 to t in Eq.(A.3), is obtained

$$\hat{\rho}^*(t) = \hat{\rho}^*(t_0) - i \int_{t_0}^t dt' [\hat{\mathcal{H}}_I(t'), \hat{\rho}^*(t')], \quad (\text{A.4})$$

which, inserted in Eq. (A.3),

$$\frac{d}{dt} \hat{\rho}^*(t) = -i [\hat{\mathcal{H}}_I(t), \hat{\rho}^*(t_0)] - \int_{t_0}^t dt' [\hat{\mathcal{H}}_I(t), [\hat{\mathcal{H}}_I(t'), \hat{\rho}^*(t')]], \quad (\text{A.5})$$

add a term in second power of $\hat{\mathcal{H}}_I$.

Writing the density operator as Eq. (3.1), the conducting array dynamics from the Eq. (A.5) gives

$$\frac{d}{dt}\hat{\rho}_C(t) = - \int_{t_0}^t dt' \text{Tr}_E \left[\hat{\mathcal{H}}_I(t), \left[\hat{\mathcal{H}}_I(t'), \hat{\rho}_C(t') \otimes \hat{\rho}_E \right] \right], \quad (\text{A.6})$$

where it was verified

$$\text{Tr}_E[\hat{\mathcal{H}}_I(t), \hat{\rho}_C(t_0) \otimes \hat{\rho}_E] = 0, \quad (\text{A.7})$$

because of the form of $\hat{\mathcal{H}}_I$ (see Eq. (2.54)) and $\hat{\rho}_E$ (see Eq. (3.2)).

Considering Markov approximation ($\hat{\rho}_C(t') \approx \hat{\rho}_C(t)$) and the transformation $t' = t - \tau$, the Eq. (A.6) becomes

$$\frac{d}{dt}\hat{\rho}_C(t) = - \int_0^\infty d\tau \text{Tr}_E \left[\hat{\mathcal{H}}_I(t), \left[\hat{\mathcal{H}}_I(t - \tau), \hat{\rho}_C(t) \otimes \hat{\rho}_E \right] \right], \quad (\text{A.8})$$

where the integral was extended to $t - t_0 \rightarrow \infty$ because of the low correlation decay time.

Writing the conducting array dynamics in the Schrödinger picture, is obtained the Redfield equation shown in Eq. (3.3) [Breuer et al., 2002, Timm, 2008].

Appendix B

Lindblad quantum master equation

Consider the conducting array Hamiltonian $\hat{\mathcal{H}}_C$ in terms of the eigenstates as Eq. (2.38); the reservoir Hamiltonians from Eq. (3.2),

$$\hat{\mathcal{H}}_\lambda = \sum_x \omega_x \hat{u}_{\lambda,x}^\dagger \hat{u}_{\lambda,x}, \quad (\text{B.1})$$

written in terms of annihilation and creation operators, $\hat{u}_{\lambda,x}$ and $\hat{u}_{\lambda,x}^\dagger$, respectively, of particles at the reservoir λ and mode x with energy ω_x ; and the interaction Hamiltonian $\hat{\mathcal{H}}_I$ from Eq. (2.54) in separable form as

$$\hat{\mathcal{H}}_I = \sum_\lambda \left(\hat{S}_\lambda \hat{\mathcal{R}}_\lambda + \hat{S}_\lambda^\dagger \hat{\mathcal{R}}_\lambda^\dagger \right), \quad \hat{\mathcal{H}}_I(t) = \sum_\lambda \left(\hat{S}_\lambda(t) \hat{\mathcal{R}}_\lambda(t) + \hat{S}_\lambda^\dagger(t) \hat{\mathcal{R}}_\lambda^\dagger(t) \right), \quad (\text{B.2})$$

in the Schrödinger and interaction picture (transformation in Eq. (A.2)), respectively, where the conducting array part \hat{S}_λ (see Table B.1) could be written in terms of conducting array eigenstates as

$$\hat{S}_\lambda = \sum_{n,m} \mathcal{S}_\lambda^{(n,m)} \hat{L}_{n,m}, \quad \hat{S}_\lambda(t) = \sum_{n,m} \mathcal{S}_\lambda^{(n,m)} \exp(i\omega_{n,m}t) \hat{L}_{n,m}, \quad (\text{B.3})$$

whit $\mathcal{S}_\lambda^{(n,m)} = \langle e_n | \hat{S}_\lambda | e_m \rangle$, $\hat{L}_{n,m} = |e_n\rangle \langle e_m|$ and $\omega_{n,m} = \omega_n - \omega_m$, while the reservoir part (see Table B.1) has a form

$$\hat{\mathcal{R}}_\lambda = \sum_x V_x^{(\lambda)} \hat{u}_{\lambda,x}, \quad \hat{\mathcal{R}}_\lambda(t) = \sum_x V_x^{(\lambda)} \exp(-i\omega_x t) \hat{u}_{\lambda,x}, \quad (\text{B.4})$$

whit $V_x^{(\lambda)}$ the coupling constants of mode x and reservoir λ .

Table B.1: Conducting array part, \hat{S}_λ , and reservoir part, $\hat{\mathcal{R}}_\lambda$, of interaction Hamiltonians in Eq. (2.54).

Reservoir (λ)	Conducting array part (\hat{S}_λ)	Reservoir part ($\hat{\mathcal{R}}_\lambda$)
Left lead	$\sum_{i,\alpha} u_i^{(L)} \hat{c}_{i,\alpha}^\dagger$	$\sum_k V_k^{(L)} \hat{c}_{L,k}$
Right lead	$\sum_{i,\alpha} u_i^{(R)} \hat{c}_{i,\alpha}^\dagger$	$\sum_k V_k^{(R)} \hat{c}_{R,k}$
Radiation	$\sum_{i,\alpha > \alpha'} u_i^{(\text{rad})} \hat{c}_{i,\alpha}^\dagger \hat{c}_{i,\alpha'}$	$\sum_p V_p^{(\text{rad})} \hat{a}_{\text{rad},p}$
Phonon	$\sum_{i,\alpha} u_i^{(\text{ph})} \hat{c}_{i,\alpha}^\dagger \hat{c}_{i,\alpha}$	$\sum_q V_q^{(\text{rad})} \hat{a}_{\text{ph},q}$

The environment density operator $\hat{\rho}_E$ in Eq. (3.2), describes any reservoir λ as thermal density operators (see Sec. 2.1.4)

$$\hat{\rho}_\lambda = \begin{cases} \frac{\exp(-\beta_0(\hat{\mathcal{H}}_\lambda - \mu_\lambda \hat{\mathcal{N}}_\lambda))}{Z}, & \mathcal{Z} = \prod_x (1 + \exp(-\beta_0(\omega_x - \mu_\lambda)))^{-1}, \quad \text{Fermions} \\ \frac{\exp(-\beta_0 \hat{\mathcal{H}}_\lambda)}{Z}, & Z = \prod_x (1 - \exp(-\beta_0 \omega_x))^{-1}, \quad \text{Bosons} \end{cases} \quad (\text{B.5})$$

for fermion and boson reservoirs, respectively, where the number operator of particles in the reservoir λ is written as

$$\hat{\mathcal{N}}_\lambda = \sum_x \hat{u}_{\lambda,x}^\dagger \hat{u}_{\lambda,x}. \quad (\text{B.6})$$

Based on the interaction Hamiltonian in Eq. (B.2), the term

$$I = \text{Tr}_E \left[\hat{\mathcal{H}}_I, \left[\hat{\mathcal{H}}_I(-\tau), \hat{\rho}_C \otimes \hat{\rho}_E \right] \right] \quad (\text{B.7})$$

from the Redfield equation in Eq. (3.3) becomes

$$I = \sum_\lambda \left[\left(\hat{S}_\lambda^\dagger \hat{S}_\lambda(-\tau) \hat{\rho}_C - \hat{S}_\lambda(-\tau) \hat{\rho}_C \hat{S}_\lambda^\dagger \right) C_\lambda(\tau) + \left(\hat{\rho}_C \hat{S}_\lambda^\dagger(-\tau) \hat{S}_\lambda - \hat{S}_\lambda \hat{\rho}_C \hat{S}_\lambda^\dagger(-\tau) \right) C_\lambda(-\tau) \right. \\ \left. + \left(\hat{S}_\lambda \hat{S}_\lambda^\dagger(-\tau) \hat{\rho}_C - \hat{S}_\lambda^\dagger(-\tau) \hat{\rho}_C \hat{S}_\lambda \right) \tilde{C}_\lambda(\tau) + \left(\hat{\rho}_C \hat{S}_\lambda(-\tau) \hat{S}_\lambda^\dagger - \hat{S}_\lambda^\dagger \hat{\rho}_C \hat{S}_\lambda(-\tau) \right) \tilde{C}_\lambda(-\tau) \right], \quad (\text{B.8})$$

where has been defined the reservoir correlation functions,

$$C_\lambda(\tau) = \langle \hat{\mathcal{R}}_\lambda^\dagger \hat{\mathcal{R}}_\lambda(-\tau) \rangle = \sum_x |V_x^{(\lambda)}|^2 \exp(i\omega_x \tau) \text{Tr}_\lambda \left[\hat{\rho}_\lambda \hat{u}_{\lambda,x}^\dagger \hat{u}_{\lambda,x} \right], \\ \tilde{C}_\lambda(\tau) = \langle \hat{\mathcal{R}}_\lambda \hat{\mathcal{R}}_\lambda^\dagger(-\tau) \rangle = \sum_x |V_x^{(\lambda)}|^2 \exp(-i\omega_x \tau) \text{Tr}_\lambda \left[\hat{\rho}_\lambda \hat{u}_{\lambda,x} \hat{u}_{\lambda,x}^\dagger \right]. \quad (\text{B.9})$$

With the thermal density operators in Eq. (B.5), the correlations in Eq. (B.9) are reduced to

$$C_\lambda(\tau) = \langle \hat{\mathcal{R}}_\lambda^\dagger \hat{\mathcal{R}}_\lambda(-\tau) \rangle = \begin{cases} \sum_x |V_x^{(\lambda)}|^2 f_\lambda^{(x)} \exp(i\omega_x \tau), & \text{Fermions} \\ \sum_x |V_x^{(\lambda)}|^2 n_\lambda^{(x)} \exp(i\omega_x \tau), & \text{Bosons} \end{cases} \quad (\text{B.10})$$

$$\tilde{C}_\lambda(\tau) = \langle \hat{\mathcal{R}}_\lambda \hat{\mathcal{R}}_\lambda^\dagger(-\tau) \rangle = \begin{cases} \sum_x |V_x^{(\lambda)}|^2 \tilde{f}_\lambda^{(x)} \exp(-i\omega_x \tau), & \text{Fermions} \\ \sum_x |V_x^{(\lambda)}|^2 \tilde{n}_\lambda^{(x)} \exp(-i\omega_x \tau), & \text{Bosons} \end{cases}$$

where has been defined the fermion and boson density,

$$f_\lambda(\omega_x) \equiv f_\lambda^{(x)} = 1 - \tilde{f}_\lambda^{(x)} = (\exp(\beta_0(\omega_x - \mu_\lambda)) + 1)^{-1}, \quad (\text{B.11})$$

$$n_\lambda(\omega_x) \equiv n_\lambda^{(x)} = \tilde{n}_\lambda^{(x)} - 1 = (\exp(\beta_0 \omega_x) - 1)^{-1},$$

respectively, at energy ω_x .

With conducting array part in Eq. (B.3) and correlations in Eq. (B.10), the term I in Eq. (B.8) becomes

$$I = \sum_\lambda \sum_{n,m,i,j} \mathcal{S}_\lambda^{(n,m)} \mathcal{S}_\lambda^{(i,j)*} \left[\left(\hat{L}_{i,j}^\dagger \hat{L}_{n,m} \hat{\rho}_C - \hat{L}_{n,m} \hat{\rho}_C \hat{L}_{i,j}^\dagger \right) C_\lambda(\tau) \exp(-i\omega_{n,m}\tau) \right. \\ \left. + \left(\hat{\rho}_C \hat{L}_{i,j}^\dagger \hat{L}_{n,m} - \hat{L}_{n,m} \hat{\rho}_C \hat{L}_{i,j}^\dagger \right) C_\lambda(-\tau) \exp(i\omega_{i,j}\tau) \right. \\ \left. + \left(\hat{L}_{n,m} \hat{L}_{i,j}^\dagger \hat{\rho}_C - \hat{L}_{i,j}^\dagger \hat{\rho}_C \hat{L}_{n,m} \right) \tilde{C}_\lambda(\tau) \exp(i\omega_{i,j}\tau) \right. \\ \left. + \left(\hat{\rho}_C \hat{L}_{n,m} \hat{L}_{i,j}^\dagger - \hat{L}_{i,j}^\dagger \hat{\rho}_C \hat{L}_{n,m} \right) \tilde{C}_\lambda(-\tau) \exp(-i\omega_{n,m}\tau) \right], \quad (\text{B.12})$$

which, in the interaction picture,

$$I' = \sum_\lambda \sum_{n,m,i,j} \mathcal{S}_\lambda^{(n,m)} \mathcal{S}_\lambda^{(i,j)*} \exp(i(\omega_{n,m} - \omega_{i,j})t) \left[\left(\hat{L}_{i,j}^\dagger \hat{L}_{n,m} \hat{\rho}_C - \hat{L}_{n,m} \hat{\rho}_C \hat{L}_{i,j}^\dagger \right) C_\lambda(\tau) \exp(-i\omega_{n,m}\tau) \right. \\ \left. + \left(\hat{\rho}_C \hat{L}_{i,j}^\dagger \hat{L}_{n,m} - \hat{L}_{n,m} \hat{\rho}_C \hat{L}_{i,j}^\dagger \right) C_\lambda(-\tau) \exp(i\omega_{i,j}\tau) \right. \\ \left. + \left(\hat{L}_{n,m} \hat{L}_{i,j}^\dagger \hat{\rho}_C - \hat{L}_{i,j}^\dagger \hat{\rho}_C \hat{L}_{n,m} \right) \tilde{C}_\lambda(\tau) \exp(i\omega_{i,j}\tau) \right. \\ \left. + \left(\hat{\rho}_C \hat{L}_{n,m} \hat{L}_{i,j}^\dagger - \hat{L}_{i,j}^\dagger \hat{\rho}_C \hat{L}_{n,m} \right) \tilde{C}_\lambda(-\tau) \exp(-i\omega_{n,m}\tau) \right], \quad (\text{B.13})$$

oscillates as a function of time with frequency $\omega_{n,m} - \omega_{i,j}$, at least $n = i$ and $m = j$ as secular approximation.

The reconstruction of the Redfield equation needs to integrate the correlation functions, which,

Table B.2: Effective transfer rates, $\kappa_\lambda^{(n,m)}$ and $\tilde{\kappa}_\lambda^{(n,m)}$, for reservoir λ .

λ	$\kappa_\lambda^{(n,m)}$	$\tilde{\kappa}_\lambda^{(n,m)}$
L	$\gamma_L^{(n,m)} f_L^{(n,m)} \langle e_n \sum_{i,\alpha} u_i^{(L)} \hat{c}_{i,\alpha}^\dagger e_m \rangle ^2$	$\gamma_L^{(n,m)} \tilde{f}_L^{(n,m)} \langle e_n \sum_{i,\alpha} u_i^{(L)} \hat{c}_{i,\alpha}^\dagger e_m \rangle ^2$
R	$\gamma_R^{(n,m)} f_R^{(n,m)} \langle e_n \sum_{i,\alpha} u_i^{(R)} \hat{c}_{i,\alpha}^\dagger e_m \rangle ^2$	$\gamma_R^{(n,m)} \tilde{f}_R^{(n,m)} \langle e_n \sum_{i,\alpha} u_i^{(R)} \hat{c}_{i,\alpha}^\dagger e_m \rangle ^2$
rad	$\gamma_{\text{rad}}^{(n,m)} n_{\text{rad}}^{(n,m)} \langle e_n \sum_{i,\alpha>\alpha} u_i^{(\text{rad})} \hat{c}_{i,\alpha}^\dagger \hat{c}_{i,\alpha} e_m \rangle ^2$	$\gamma_{\text{rad}}^{(n,m)} \tilde{n}_{\text{rad}}^{(n,m)} \langle e_n \sum_{i,\alpha>\alpha} u_i^{(\text{rad})} \hat{c}_{i,\alpha}^\dagger \hat{c}_{i,\alpha} e_m \rangle ^2$
ph	$\gamma_{\text{ph}}^{(n,m)} n_{\text{ph}}^{(n,m)} \langle e_n \sum_{i,\alpha} u_i^{(\text{ph})} \hat{c}_{i,\alpha}^\dagger \hat{c}_{i,\alpha} e_m \rangle ^2$	$\gamma_{\text{ph}}^{(n,m)} \tilde{n}_{\text{ph}}^{(n,m)} \langle e_n \sum_{i,\alpha} u_i^{(\text{ph})} \hat{c}_{i,\alpha}^\dagger \hat{c}_{i,\alpha} e_m \rangle ^2$

through the Cauchy principal value theorem, are

$$\int_0^\infty d\tau C_\lambda(\pm\tau) \exp(\mp i\omega_{n,m}\tau) = \begin{cases} \frac{1}{2} \gamma_\lambda^{(n,m)} f_\lambda^{(n,m)}, & \text{Fermions} \\ \frac{1}{2} \gamma_\lambda^{(n,m)} n_\lambda^{(n,m)}, & \text{Bosons} \end{cases} \quad (\text{B.14})$$

$$\int_0^\infty d\tau \tilde{C}_\lambda(\pm\tau) \exp(\pm i\omega_{n,m}\tau) = \begin{cases} \frac{1}{2} \gamma_\lambda^{(n,m)} \tilde{f}_\lambda^{(n,m)}, & \text{Fermions} \\ \frac{1}{2} \gamma_\lambda^{(n,m)} \tilde{n}_\lambda^{(n,m)}, & \text{Bosons} \end{cases}$$

where has been defined the spectral density,

$$\gamma_\lambda(\omega) = \pi \sum_x |V_x^{(\lambda)}|^2 \delta(\omega - \omega_x), \quad (\text{B.15})$$

such $\gamma_\lambda^{(n,m)} = \gamma_\lambda(\omega_{n,m})$ is the spectral density at transition frequency $\omega_{n,m}$, and the typical Lamp shift has been ignored.

Writing I , from Eq. (B.12), in the secular approximation and the integrated correlation functions as Eq. (B.14), the Redfield equation becomes in the Lindblad quantum master equation shown in Eq. (3.4), where the *effective transfer rates*, $\kappa_\lambda^{(n,m)}$ and $\tilde{\kappa}_\lambda^{(n,m)}$, are shown in the Table B.2.

Appendix C

Reservoir particles evolution

The evolution of the nanojunction density operator $\hat{\rho}$ in the Schrödinger picture and Markov approximation, from the Eq. (A.5), is given by

$$\frac{d}{dt}\hat{\rho} = -i \left[\hat{\mathcal{H}}_C, \hat{\rho} \right] - i \hat{U}^\dagger \left[\hat{\mathcal{H}}_I(t), \hat{\rho}(t_0) \right] \hat{U} - \int_0^\infty d\tau \left[\hat{\mathcal{H}}_I \left[\hat{\mathcal{H}}_I(-\tau), \hat{\rho} \right] \right], \quad (\text{C.1})$$

where \hat{U} was defined in Eq. (A.2). With $\hat{\mathcal{N}}_\lambda$ the number operator of particle in the reservoir λ (see Eq. (B.6)), based on the Eq. (C.1), the variation of particles is given by,

$$\frac{d}{dt}\langle \hat{\mathcal{N}}_\lambda \rangle = -\text{Tr} \left[\hat{\mathcal{N}}_\lambda \int_0^\infty d\tau \left[\hat{\mathcal{H}}_I, \left[\hat{\mathcal{H}}_I(-\tau), \hat{\rho}_C \otimes \rho_E \right] \right] \right], \quad (\text{C.2})$$

where Tr performs the trace over the conducting array and the environment.

With the interaction Hamiltonian $\hat{\mathcal{H}}_I$ in Eq. (B.2), the Eq. (C.2) becomes

$$\begin{aligned} \frac{d}{dt}\langle \hat{\mathcal{N}}_\lambda \rangle = & - \int_0^\infty d\tau \text{Tr}_C \left[\left(\hat{\mathcal{S}}_\lambda^\dagger \hat{\mathcal{S}}_\lambda(-\tau) \hat{\rho}_C \right) C_\lambda(\tau) + \left(\hat{\rho}_C \hat{\mathcal{S}}_\lambda^\dagger(-\tau) \hat{\mathcal{S}}_\lambda \right) C_\lambda(-\tau) \right. \\ & \left. - \left(\hat{\mathcal{S}}_\lambda^\dagger(-\tau) \hat{\rho}_C \hat{\mathcal{S}}_\lambda \right) \tilde{C}_\lambda(\tau) - \left(\hat{\mathcal{S}}_\lambda^\dagger \hat{\rho}_C \hat{\mathcal{S}}_\lambda(-\tau) \right) \tilde{C}_\lambda(-\tau) \right], \end{aligned} \quad (\text{C.3})$$

where the correlations where defined in Eq. (B.10). Writting the conducting array part as Eq. (B.3) and the principal value theorem in Eq. (B.14), the Eq. (C.3) in secular approximation is,

$$\frac{d}{dt}\langle \hat{\mathcal{N}}_\lambda \rangle = - \sum_{n,m} \text{Tr}_C \left[\frac{\kappa_\lambda^{(n,m)}}{2} \left(\hat{L}_{n,m}^\dagger \hat{L}_{n,m} \hat{\rho}_C + \hat{\rho}_C \hat{L}_{n,m}^\dagger \hat{L}_{n,m} \right) - \tilde{\kappa}_\lambda^{(n,m)} \hat{L}_{n,m}^\dagger \hat{\rho}_C \hat{L}_{n,m} \right], \quad (\text{C.4})$$

where the effective transfer rates $\kappa_\lambda^{(n,m)}$ and $\tilde{\kappa}_\lambda^{(n,m)}$ are shown in Table B.2. Tracing over the conducting array degrees of freedom, the Eq. (C.4) becomes

$$\frac{d}{dt}\langle \hat{\mathcal{N}}_\lambda \rangle = - \sum_{n,m} \left(\kappa_\lambda^{(n,m)} \rho_m - \tilde{\kappa}_\lambda^{(n,m)} \rho_n \right). \quad (\text{C.5})$$